JACS JOURNAL OF THE AMERICAN CHEMICAL SOCIETY

Article

Cite This: J. Am. Chem. Soc. 2019, 141, 7333−7346

pubs.acs.org/JACS

# Stabilization of O−O Bonds by $d^0$ Cations in $Li_{4+x}Ni_{1-x}WO_6$ ($0 \le x \le 0.25$) Rock Salt Oxides as the Origin of Large Voltage Hysteresis

Zoe N. Taylor,[†] Arnaud J. Perez,[†] José A. Coca-Clemente,[†,‡] Filipe Braga,[†,‡] Nicholas E. Drewett,[†,‡,⊥] Michael J. Pitcher,[†] William J. Thomas,[†] Matthew S. Dyer,[†] Christopher Collins,[†] Marco Zanella,[†] Timothy Johnson,[†] Sarah Day,[§] Chiu Tang,[§] Vinod R. Dhanak,[‡,∥] John B. Claridge,[†] Laurence J. Hardwick,[†,‡] and Matthew J. Rosseinsky*[,†]

[†]Department of Chemistry and [∥]Department of Physics, University of Liverpool, Crown Street, Liverpool L69 7ZD, United Kingdom

[‡]Stephenson Institute for Renewable Energy, University of Liverpool, Chadwick Building, Peach Street, Liverpool L69 7ZF, United Kingdom

[§]Diamond Light Source, Diamond House, Harwell Oxford, Didcot, Oxfordshire OX11 0DE, United Kingdom

Supporting Information

**ABSTRACT:** Multinary lithium oxides with the rock salt structure are of technological importance as cathode materials in rechargeable lithium ion batteries. Current state-of-the-art cathodes such as $LiNi_{1/3}Mn_{1/3}Co_{1/3}O_2$ rely on redox cycling of earth-abundant transition-metal cations to provide charge capacity. Recently, the possibility of using the oxide anion as a redox center in Li-rich rock salt oxides has been established as a new paradigm in the design of cathode materials with enhanced capacities (>200 mAh/g). To increase the lithium content and access electrons from oxygen-derived states, these materials typically require transition metals in high oxidation states, which can be easily achieved using $d^0$ cations. However, Li-rich rock salt oxides with high valent $d^0$ cations such as $Nb^{5+}$ and $Mo^{6+}$ show strikingly high voltage hysteresis between charge and discharge, the origin of which is uninvestigated. In this work, we study a series of Li-rich compounds, $Li_{4+x}Ni_{1-x}WO_6$ ($0 \le x \le 0.25$) adopting two new and distinct cation-ordered variants of the rock salt structure. The $Li_{4.15}Ni_{0.85}WO_6$ ($x = 0.15$) phase has a large reversible capacity of 200 mAh/g, without accessing the $Ni^{3+}/Ni^{4+}$ redox couple, implying that more than two-thirds of the capacity is due to anionic redox, with good cyclability. The presence of the $5d^0$ $W^{6+}$ cation affords extensive (>2 V) voltage hysteresis associated with the anionic redox. We present experimental evidence for the formation of strongly stabilized localized O−O single bonds that explain the energy penalty required to reduce the material upon discharge. The high valent $d^0$ cation associates localized anion−anion bonding with the anion redox capacity.

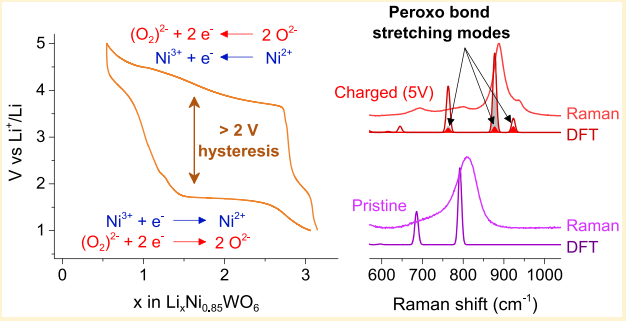


## INTRODUCTION

Li-containing rock salt oxides form one of the most studied families of positive electrodes for rechargeable lithium ion batteries. Following the success of the first commercial Li-ion systems using $LiCoO_2$ as a cathode material, extensive exploration of other $LiMO_2$ analogues has led to the discovery of higher-performing materials, among which are the current state-of-the-art NMC phases ($LiNi_xMn_yCo_{1-x-y}O_2$). The maximum capacity of these materials is, however, still limited because of the 1:1 Li:M ratio, and great hope is being placed in the "Li-rich" rock salt oxides ($Li_xM_yO_{x+y}$ with $x > y$) which can be accessed by partial substitution of the transition metal with excess Li associated with an increase in the mean metal oxidation state above +III (e.g., $Li(Li_{1/3}Mn_{2/3})O_2$ or $Li_2MnO_3$). Such compounds can deliver capacities exceeding 200 mAh/g, making them promising cathode materials for future Li-ion rechargeable batteries. These capacities exceed expectations based on purely metal-based redox within the expected manifold of oxidation states in cathode materials with Li/M > 1. This is now well understood as the contribution of oxygen to the redox activity, made possible by the presence of nonbonding oxygen states close to the Fermi level in Li-rich rock salt oxides because some O 2p orbitals do not take part in the formation of M−O bonding and antibonding orbitals.[1−3] Oxygen-based redox reversibility can be enhanced by moving from 3d to 4d and 5d cations, which avoids the formation of gaseous $O_2$ upon anion oxidation.[4] Chemistries that enable reversible oxygen oxidation with earth-abundant components would bring these capacities within practical reach.

Despite their large diversity of structures and compositions, few Li-rich rock salt oxides have been studied as cathode

Received: December 21, 2018
Published: April 11, 2019




DOI: 10.1021/jacs.8b13633
J. Am. Chem. Soc. 2019, 141, 7333−7346

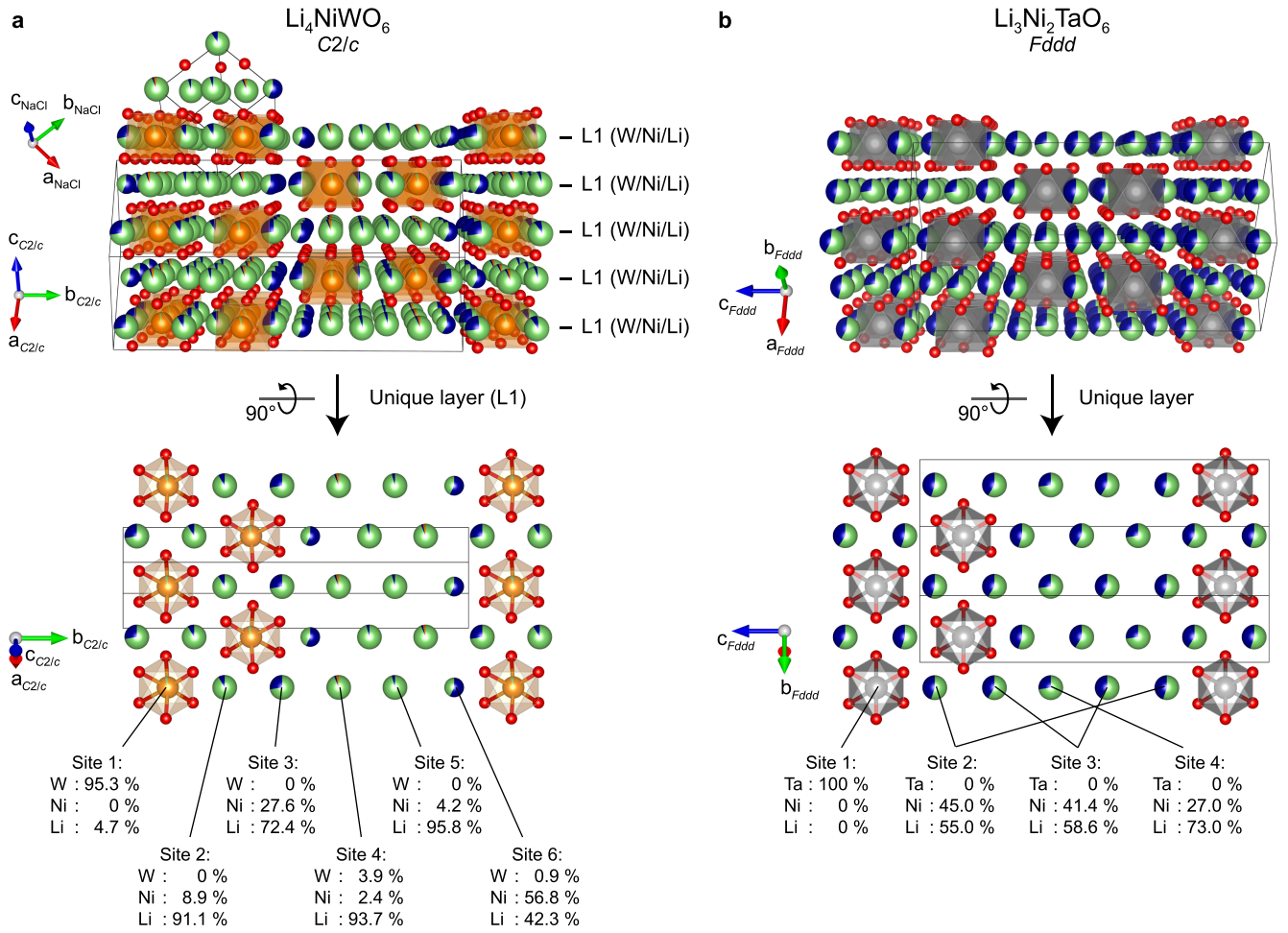


**Figure 1.** Structure of $Li_4NiWO_6$. Comparison of the *C*2/*c* structure of stoichiometric $Li_4NiWO_6$ (a) and the *Fddd* structure of the archetype $Li_3Ni_2TaO_6$ (b) phases. For $Li_4NiWO_6$, the cubic unit cell of the NaCl structure is shown in addition to the *C*2/*c* cell to highlight the rock salt ordering of the structure. Both structures can be described by a staggered stacking sequence of a unique layer with a similar ordering of the highest oxidation state cation ($W^{6+}$ in orange and $Ta^{5+}$ in gray). The unique layer for each structure is rotated by 90° and displayed in the lower part of the figure. The different contents of Ni (blue) and Li (green) coupled with the off-center displacement of $W^{6+}$ result in different orderings of the remaining cation sites in the two materials, with site 2 (site 3) of the *Fddd* structure being split into sites 2 and 6 (sites 3 and 5) of the *C*2/*c* structure. The partial occupation of the different cation sites is indicated in the figure.

materials. By carefully selecting the transition metals used, these compounds can exhibit complex cation-ordered superstructures[5−8] and their Li content can be varied extensively ($LiMO_2 \rightarrow Li_2MO_3 \rightarrow Li_3MO_4 \rightarrow Li_4MO_5$...),[9,10] resulting in a considerable diversity of candidates for new cathode materials and a great opportunity to explore the role played by different cations in triggering oxygen redox. Following this idea, Yabuuchi and co-workers have shown the possibility of using a high-valence $d^0$ cation such as $Nb^{5+}$ or $Mo^{6+}$ to increase the Li content in rock salt oxides, create nonbonding oxygen states close to the Fermi level and activating the redox activity of oxygen.[11,12] Interestingly, several of these materials show extremely large voltage hysteresis with most of the discharge capacity recovered below 2 V, but its origin has not been investigated so far. Although such low energy efficiency is detrimental to their use in practical Li-ion batteries, understanding the origin of this feature will help in the design of future cathode materials because the voltage hysteresis issue is pervasive in materials showing anionic redox activity, including the long-sought-after Li-rich NMC phases.[13−15]

In this work, we investigate a family of Li-rich rock salt oxides $Li_{4+x}Ni_{1-x}WO_6$ ($0 \leq x \leq 0.25$) derived from the $Li_4NiWO_6$ phase reported by Mandal et al.[16] and vary the Li/Ni ratio to tune the structural and electrochemical properties of the material. Using a combination of spectroscopic techniques (XPS, XAS, and Raman), the role of Ni and O in the charge compensation during electrochemical (de)lithiation was investigated, revealing the influence of redox-inactive $W^{6+}$ ($5d^0$) cations on the formation of stable, discrete O−O bonds upon oxidation of oxide and the associated voltage hysteresis.

## RESULTS

**Synthesis and Structure of $Li_{4+x}Ni_{1-x}WO_6$ Materials.** The initial synthesis experiments to prepare the stoichiometric $Li_4NiWO_6$ phase were carried out by a classical solid-state method using NiO, $WO_3$, and a 10% molar excess of $Li_2CO_3$ (1:1:4.4) to compensate for $Li_2O$ volatility during high-temperature synthesis (Methods). This resulted in a dark-brown powder which initially appeared pure from laboratory PXRD. However, upon further analysis by synchrotron PXRD, neutron powder diffraction, and TEM-EDX, the sample turned


DOI: 10.1021/jacs.8b13633
J. Am. Chem. Soc. 2019, 141, 7333−7346

out to be nonstoichiometric and contain a small amount of cubic $Li_{1-x}Ni_xO$ impurity, thus providing evidence for the existence of a solid solution of the form $Li_{4+x}Ni_{1-x}WO_6$. By revising the initial synthesis conditions, using different Ni/W ratios and sacrificial powder to better control the Li stoichiometry (Methods), we were able to obtain the stoichiometric pale-green $Li_4NiWO_6$ phase without impurity as well as the $Li_{4+x}Ni_{1-x}WO_6$ solid solution with $0.05 \leq x \leq 0.25$. The compositions of the different phases were confirmed by ICP−OES and TEM−EDX analysis (Note 1 in Supporting Information (SI)). Although all members of the nonstoichiometric $Li_{4+x}Ni_{1-x}WO_6$ solid solution could be approximately indexed with the structural model reported by Mandal et al.,[16] the diffraction pattern of the stoichiometric $Li_4NiWO_6$ ($x = 0$) could not be matched with the reported structure and turned out to be a new structure type. A thorough structural investigation was therefore undertaken on the $Li_4NiWO_6$ and $Li_{4.1}Ni_{0.9}WO_6$ samples using synchrotron X-ray and neutron powder diffraction data (detailed structural analysis in Notes 2 and 3 in the SI).

The structure of the stoichiometric $Li_4NiWO_6$ phase was solved in the $C2/c$ space group ($a$ = 5.84579(10) Å, $b$ = 17.58769(35) Å, $c$ = 5.109138(9) Å, $\beta$ = 124.768(1)°, $V$ = 431.506(2) Å$^3$; see Table S1 in Supporting Information for full structural parameters) and can be thought of as a monoclinic distortion of the $Li_3Ni_2TaO_6$ (*Fddd*) archetype based on the same ordering pattern of the almost fully occupied W sites, which follows that of Ta in the archetype (Figure 1b) but a different Ni/Li ordering.[17] The relationship between the two cells is shown in Figure S1 in Supporting Information. Pauling's rule of electroneutrality prevents two highly charged $W^{6+}$ cations from being coordinated to the same oxygen. In other words, $W^{6+}$ cannot be situated in the first two cation neighboring shells of any $W^{6+}$ cation at translations $\mathbf{T}_1 = (a/2, a/2, 0)$ and $\mathbf{T}_2 = (a, 0, 0)$, where $a$ is the rock salt cubic cell dimension. As a result, they form isolated $WO_6$ octahedra arranged to minimize electrostatic repulsions between $W^{6+}$ cations, separated by $\mathbf{T}_3 = (a, a/2, a/2)$ (Figure 3a), adopting 1 of the 10 such arrangements noted by Hauk et al.[18] As a consequence, all oxygen atoms in the structure are coordinated to only one W atom. $Li_3Ni_2TaO_6$ and the new $Li_4NiWO_6$ structure can be described as a staggered six-layer repeat sequence of a single mixed cation layer with six distinct octahedral sites (Figure 1, bottom). The reduction in symmetry from $Li_3Ni_2TaO_6$ to $Li_4NiWO_6$, with a lower Ni content and the higher charge of the $d^0$ $W^{6+}$ cations, arises from an enhanced Li/Ni ordering, which changes the number of distinct cation sites from four to six in $Li_4NiWO_6$ by splitting site 2 (site 3) of the *Fddd* structure (Figure 1b) into sites 2 and 6 (sites 3 and 5) of the $C2/c$ structure (Figure 1a). The $W^{6+}$ cations in $Li_4NiWO_6$ are almost fully ordered onto site 1, with 4.7% $Li^+$ on this site and the remaining 4.7% $W^{6+}$ distributed between two of the remaining five cation sites (sites 4 and 6). The $Ni^{2+}$ occupancy of all other sites is driven by their interaction with highly charged $W^{6+}$ cations in this particular arrangement. Sites 2 and 6 have only five $W^{6+}$ cations in the three neighboring cation shells at $\mathbf{T}_1$, $\mathbf{T}_2$, and $\mathbf{T}_3$ (Table S2 in Supporting Information), compared to eight for the other sites, making them more likely to contain $Ni^{2+}$ as a result of lower electrostatic repulsion. The $d^0$ configuration of $W^{6+}$ leads to asymmetric displacement from the center of its octahedron, moving away from site 6 and toward the edge shared with site 2 (Tables S3 and S4 in Supporting Information), attributed to second-order Jahn−Teller effects.[19,20] This destabilizes one site at the expense of the other, leading to a high occupation of site 6 by $Ni^{2+}$ (57%) and a low occupation of site 2 (8.9%). For the same reason, site 3 is further away from the $W^{6+}$ cations and has a higher $Ni^{2+}$ content (27.6%) compared to that of site 5 (4.2%). This contrasts with the nearly statistical distribution of cations in sites 2 and 3 in $Li_3Ni_2TaO_6$, where the $d^0$ cation has a lower charge and is not displaced from the octahedron centroid. Finally, site 4 is almost fully occupied by $Li^+$ (94%) as a result of electrostatic repulsion from its $W^{6+}$ neighbors and the large distortion enforced by the two edge-sharing and two corner-sharing neighboring $WO_6$ octahedra (Figure S2 and Table S4 in Supporting Information), which would be less favorable to high-spin $Ni^{2+}$ than the other less distorted sites. To obtain the final Rietveld fit (Figure 4a), it was necessary to include an *Fddd* minority $Li_4NiWO_6$ phase isostructural with $Li_3Ni_2TaO_6$ of refined weight fraction 11.8(6) %, which can be interpreted as either regions of lithium and nickel site disorder within the material or a consequence of small Li/Ni ordered domain sizes resulting in a significant antiphase boundary content. The asymmetric displacements of W atoms occur in opposing directions along [010] and [0$\bar{1}$0] axes, resulting in no overall dipole in the material (Figure 5a). Such displacements are absent (or disordered) in the less ordered *Fddd* analogue, where the average positions of the tungsten sites are located at the centroids of the octahedra at Wyckoff site 8*a* (which has point symmetry 222 and thus no dipole).

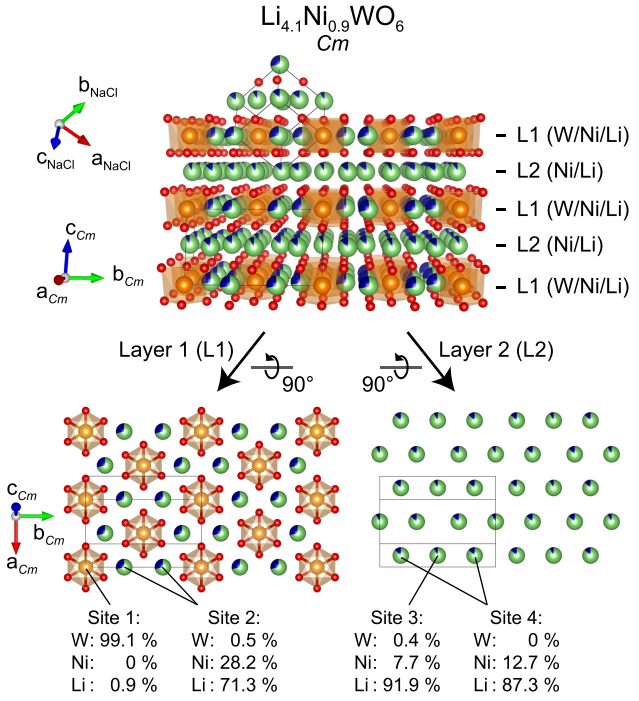


**Figure 2.** Structure of $Li_{4.1}Ni_{0.9}WO_6$. Phases with $x > 0$ in $Li_{4+x}Ni_{1-x}WO_6$, including $Li_{4.1}Ni_{0.9}WO_6$, adopt a *Cm* structure with an alternate stacking of two different layers, which are rotated by 90° and displayed in the lower part of the figure. W atoms (orange) form a honeycomb pattern in layer 1, while Ni (blue) and Li (green) occupy the other sites, with a majority of Li in layer 2 (sites 3 and 4). The partial occupation of the different cation sites is indicated in the figure. The cubic unit cell of the NaCl structure is shown in addition to the *Cm* cell to highlight the rock salt ordering of the structure.

Turning to $Li_{4.1}Ni_{0.9}WO_6$, initial peak fitting was performed on laboratory PXRD data based on the reported $Li_4NiWO_6$ cell ($a$ = 5.090(3) Å, $b$ = 8.810(4) Å, $c$ = 5.079(1) Å, $\beta$ = 109.60(5)°)[16] in the $C2/m$ space group, which accounted for all of the Bragg reflections and gave a satisfactory Le Bail fit. With



DOI: 10.1021/jacs.8b13633
J. Am. Chem. Soc. 2019, 141, 7333−7346

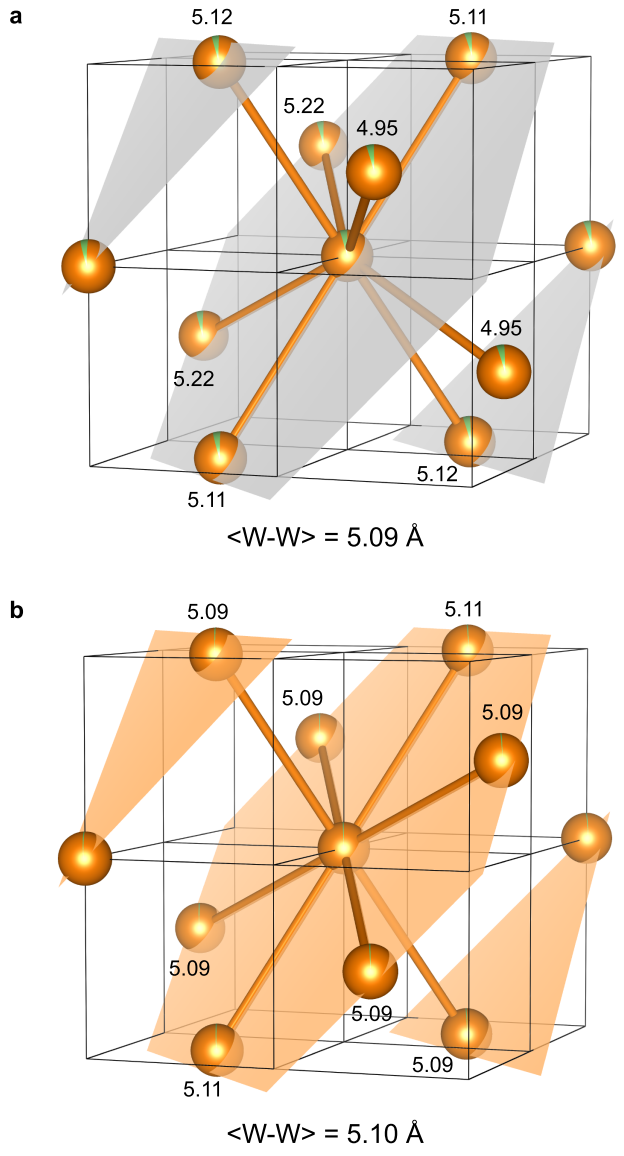


**Figure 3.** W ordering. The arrangement and distances between W atoms in $Li_4NiWO_6$ (a) and $Li_{4.1}Ni_{0.9}WO_6$ (b). The distances (in Å) from the central W atom are indicated next to each atom. The two structures have similar W−W distances, corresponding to the translation vector $\mathbf{T}_3 = (a, a/2, a/2)$, where $a$ is the dimension of the rock salt cubic cell shown in the figure. However, the ordering differs between the two structures, resulting in a layered W ordering in $Li_{4.1}Ni_{0.9}WO_6$ (b), highlighted by the orange planes, and a tridimensional W ordering for $Li_4NiWO_6$ (a), with some of the W atoms situated between the gray planes.

an increased Li content, $Li_{4.1}Ni_{0.9}WO_6$ moves further away from the $Li_3Ni_2TaO_6$ stoichiometry and adopts a monoclinic structure with four distinct cation sites, similar to the archetypal layered $Li_5ReO_6$ rock salt superstructure.[21] The $WO_6$ octahedra in $Li_{4.1}Ni_{0.9}WO_6$ are again isolated from each other, with similar W−W distances to $Li_4NiWO_6$ (Figure 3) that also correspond to the third cation shell at $\mathbf{T}_3 = (a, a/2, a/2)$ in order to minimize electrostatic repulsions but in a motif distinct from that found in $Li_4NiWO_6$. Cations order through the adoption of a two-layer structure where $(Li/Ni)O_6$ octahedra surround $WO_6$ units in a "honeycomb" arrangement in one layer (layer 1 in Figure 2), which alternates with a mixed Li/Ni layer (layer 2 in Figure 2). Ni is distributed over three of the four cation sites (sites 2, 3, and 4), with a preference for site 2 in the W layers. Site 2 has the lowest electrostatic repulsion from $W^{6+}$ cations, with only five $W^{6+}$ in the first three cation shells compared to eight for sites 3 and 4 (Table S6 in Supporting Information). This Li/Ni ordering is similar to that in related $Li_4NiMoO_6$ but differs from that in $Li_4NiTeO_6$, in which Ni is localized only at site 2.[12,22] The similar W−W network and influences on Li/Ni order suggest that the two structures are close in energy, with the increased Li content in $Li_{4.1}Ni_{0.9}WO_6$ favoring the layered structure of Li-rich $Li_5ReO_6$. Furthermore, oxygen atoms in both structures have similar coordination environments, each belonging to one $WO_6$ octahedron, although the partial Ni/Li ordering in the two materials could lead to several local coordination configurations around oxygen ($OWNiLi_4$, $OWNi_2Li_3$, or $OWLi_5$), which will necessarily have an effect on the electrochemical properties. These two variants of W ordering derived from the $C2/m$ and $Fddd$ space groups have also been reported for Os in $Li_4MgOsO_6$ and Re in $Li_4MgReO_6$,[23,24] depending on synthesis conditions. As for the $Li_{4+x}Ni_{1-x}WO_6$ system studied here, the difference between the two variants in these systems could be related to a tight balance in the Li/Mg ratio. The Rietveld model in $C2/m$ gave a poor fit to the SXRD and NPD in comparison to the Le Bail fit (Note 3 in SI). The symmetry was reduced to the noncentrosymmetric $Cm$ by the displacement of the tungsten site off-center toward one apex of the $WO_6$ octahedron (Figure 5b and Table S7 in Supporting Information), thereby removing the 2-fold rotational axis, maintaining the total number of cation sites at four but doubling the number of anion sites from two (Wyckoff sites 8$j$ and 4$i$, point symmetry 1 and $m$ respectively) to four (sites 4$b$ and 2$a$, point symmetry 1 and $m$, respectively). Here, the off-centering of W differs from that in the $C2/c$ $Li_4NiWO_6$ phase, and the displacement propagates ferrodistortively throughout the lattice, resulting in an overall permanent dipole. The final structural parameters of the combined SXRD and ND Rietveld refinement (Figure 4b), including the 2.7(2) wt % $Li_{0.3}Ni_{0.7}O$ impurity, can be found in Table S5 in Supporting Information with the final cell parameters ($a$ = 5.113747(23) Å, $b$ = 8.791326(40) Å, $c$ = 5.093213(23) Å, $\beta$ = 110.1564(12)°). While exploring the $Li_{4+x}Ni_{1-x}WO_6$ solid solution, we found that the same $Cm$ structure is preserved up to $x$ = 0.25 and observed a linear decrease in lattice parameters with increasing value of $x$ (Figure S3 in Supporting Information). This is consistent with the increasing content of smaller and more highly charged $Ni^{3+}$ when Ni is substituted by Li. For $x \geq 0.2$, impurity reflections corresponding to $Li_4WO_5$ were observed, suggesting that the limit of solid solution lies between nominal values of $0.15 \leq x \leq 0.20$.

**Electrochemical Properties.** $Li_4NiWO_6$ and $Li_{4.15}Ni_{0.85}WO_6$ (x = 0.15) samples were chosen for initial electrochemical studies in order to maximize the differences between the two structures and compositions while avoiding the presence of the $Li_4WO_5$ impurity for samples with $x \geq 0.2$. Ball milling of the active materials to reduce the particle size from 5−20 $\mu$m to 0.5−3 $\mu$m (Figure S4 in Supporting Information) was found to help both in the preparation of the casting and in achieving better electrochemical performance. The first charge/discharge cycles for the two materials are compared in Figure 6a. Both materials show very high capacities of 270 mAh/g when charged to 5 V, with some irreversible capacity on discharge. This is more pronounced for $Li_4NiWO_6$, whose reversible capacity is less than 140 mAh/g on the first cycle (52%


DOI: 10.1021/jacs.8b13633
J. Am. Chem. Soc. 2019, 141, 7333−7346

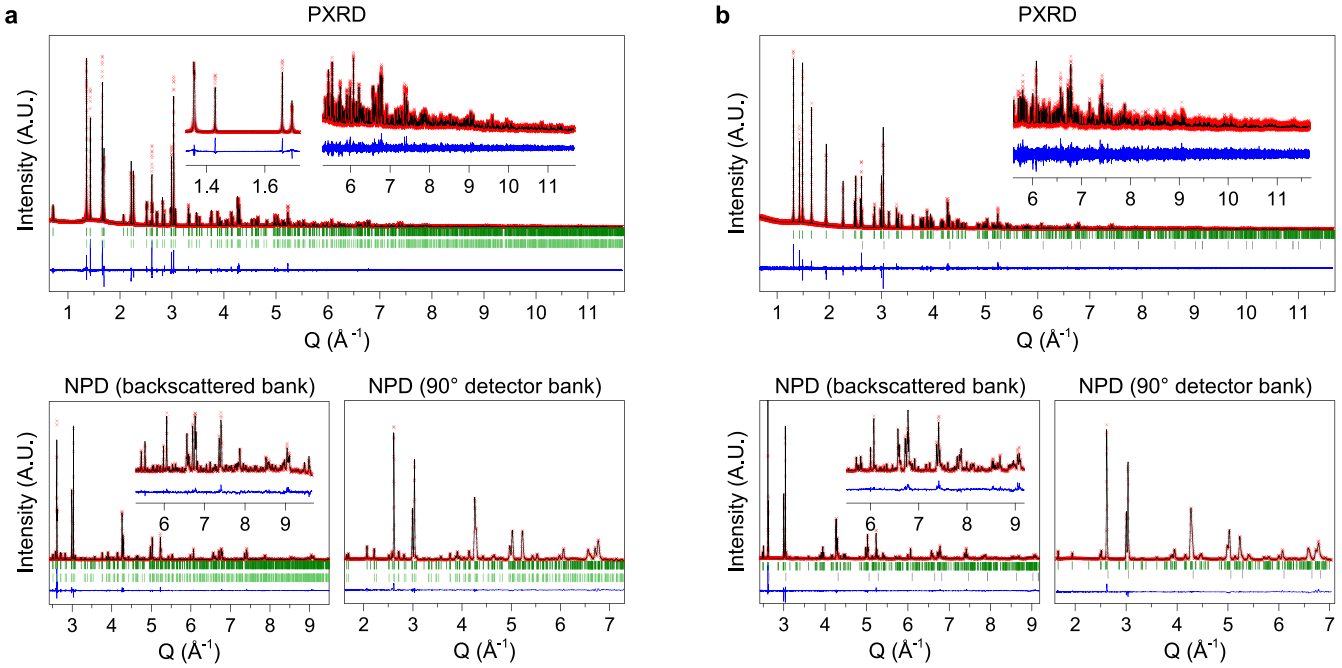


**Figure 4.** Combined Rietveld refinement of $Li_4NiWO_6$ (a) and $Li_{4.1}Ni_{0.9}WO_6$ (b) using synchrotron powder X-ray diffraction ($\lambda$ = 0.82588(1) Å) data and high-resolution neutron powder diffraction banks: a 168° bank and a 90° detector bank. Experimental points are in red, calculated patterns are in black, difference lines are in blue, *hkl* ticks are dark green for the main $Li_4NiWO_6$ (*C*2/*c*) phase and light green for the minor $Li_4NiWO_6$ (*Fddd*) phase in (a), dark green for the main $Li_{4.1}Ni_{0.9}WO_6$ (*Cm*) phase, and gray for the cubic impurity $Li_{0.3}Ni_{0.7}O$ phase in (b).

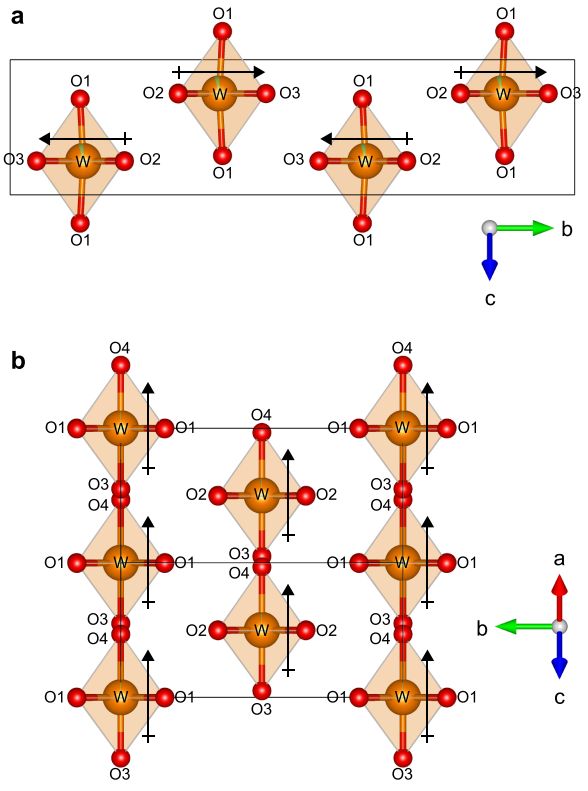


**Figure 5.** Displacement of W atoms due to a second-order Jahn−Teller effect in the two structures, resulting in overall polarization for *Cm* $Li_{4.1}Ni_{0.9}WO_6$ (b) but not for *C*2/*c* $Li_4NiWO_6$ (a).

reversibility) and decreases to 110 mAh/g on the 10th cycle, whereas a higher reversible capacity was observed for $Li_{4.15}Ni_{0.85}WO_6$ with 200 mAh/g on the first discharge (74% reversibility), decreasing to 150 mAh/g after 10 cycles (Figure 6b). Except for the lower reversible capacity of the stoichiometric phase, which could simply be related to the higher amount of Ni it contains, both materials show very similar features on charge/discharge, suggesting similar redox processes. This is particularly clear when comparing the differential capacity curves of the two materials for the first two cycles (Figure S5 in Supporting Information). Because $Li_{4.15}Ni_{0.85}WO_6$ displays a higher capacity and its structure is comparable to that of previously investigated materials,[12,22] further characterizations were performed on this sample only.

Figure 6c shows the differential capacity curve of the first and second cycles of $Li_{4.15}Ni_{0.85}WO_6$, with three redox processes occurring at 3.7, 4.2, and 4.7 V vs $Li^+/Li$ on the first charge and most of the redox activity on discharge happening at 1.7 V. Such a large voltage hysteresis (2 to 3 V) is uncommon for rock salt oxide cathode materials and was therefore investigated further. In the next cycles, different processes are observed, with ∼0.35 $Li^+$ deintercalated at 2 V and the remaining 2.25 $Li^+$ at 3.7 and 4.4 V. The irreversible capacity on the first cycle and subsequent modification of the voltage−capacity curve indicate a change in the material upon initial charging, similar to the first activation cycle of most Li-rich rock salt oxides, including Li-rich NMC,[25] which could be related to a rearrangement of cations or oxygen release from the material. To understand the origin of the irreversibility, several cells were cycled with different maximum cutoff voltages, as shown in Figure 6d, with the corresponding differential capacity curves in Figure S6 in Supporting Information. For a 4 V cutoff, less than 100 mV polarization is observed between the oxidation and reduction processes, and the discharge capacity of 100 mAh/g slightly exceeds the charge capacity of 85 mAh/g, suggesting that extra lithium is inserted upon reduction of the material at low voltage. Excess electrochemical insertion of lithium is not uncommon in rock salt oxides[3,26,27] and can be expected here by the partial



DOI: 10.1021/jacs.8b13633
J. Am. Chem. Soc. 2019, 141, 7333−7346

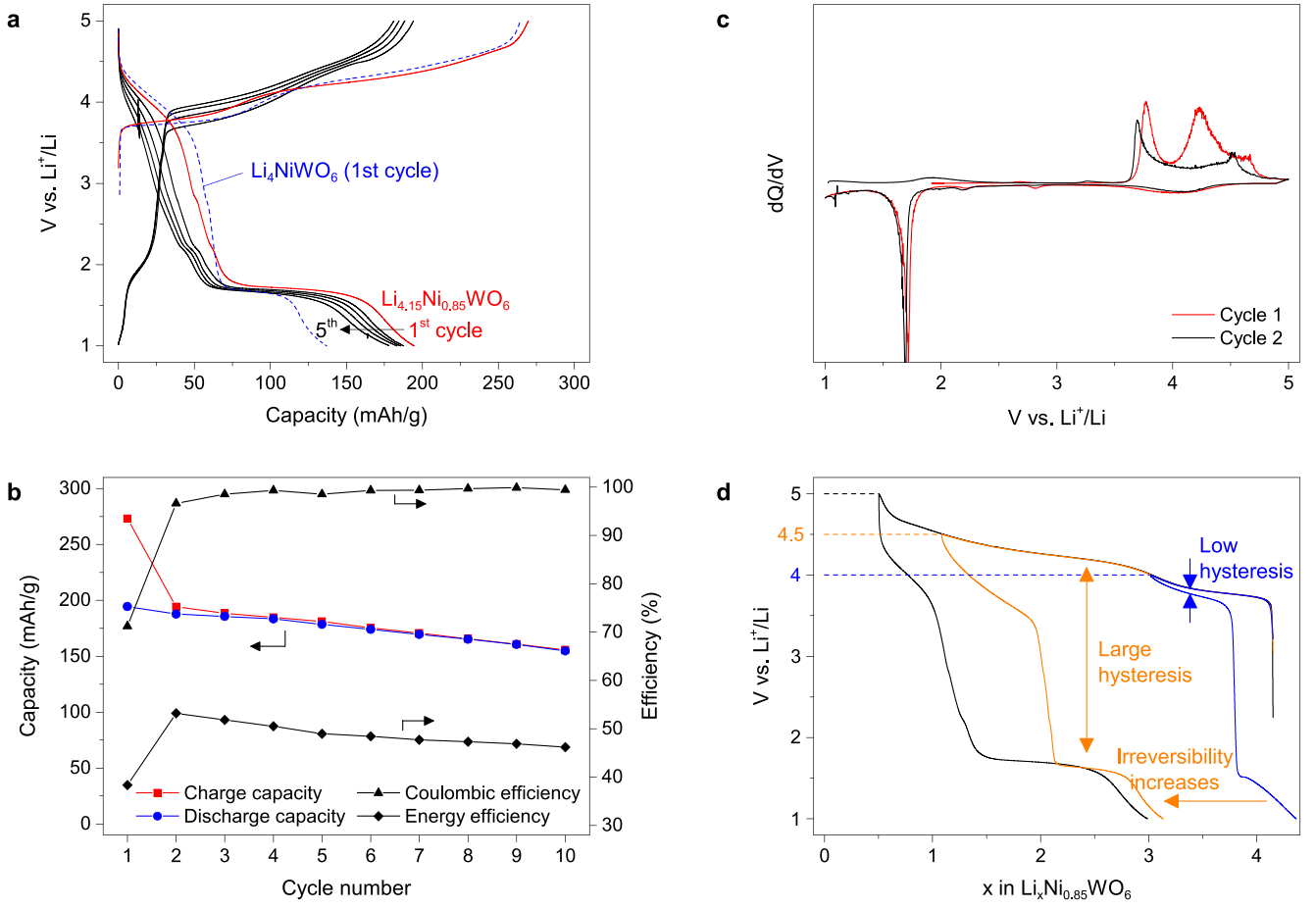


**Figure 6.** Electrochemical performance of $Li_{4+x}Ni_{1-x}WO_6$ as a cathode material. (a) First five cycles of the $Li_{4.15}Ni_{0.85}WO_6$ cathode. The first cycle of the stoichiometric $Li_4NiWO_6$ is plotted as a comparison (dashed blue line). Similar redox features are observed, but a higher reversible capacity is found for the nonstoichiometric $Li_{4.15}Ni_{0.85}WO_6$ phase. (b) Capacity retention, Coulombic efficiency, and energy efficiency for $Li_{4.15}Ni_{0.85}WO_6$. (c) Differential capacity curve for the first two cycles of $Li_{4.15}Ni_{0.85}WO_6$. (d) Voltage opening experiment. Charging to 4 V results in good reversibility of the capacity and low hysteresis whereas activation of the 4.2 V process leads to irreversible capacity and high voltage hysteresis on discharge.

oxidation of nickel in the pristine material ($Li_{4.15}Ni^{3+}{}_{0.15}Ni^{2+}{}_{0.7}WO_6$), which upon reduction can lead to the insertion of an extra $0.15Li^+$. After charging at 4.5 V with a capacity of 225 mAh/g, several broad reduction peaks are spread between 3.4 and 4.4 V, and an intense peak appears at 1.7 V corresponding to the low-voltage plateau described previously. The modification is even more obvious when the material is fully charged to 5 V, with only a broad reduction feature left at 4 V and most of the capacity recovered on the 1.7 V plateau. One can note the appearance of two small features at 2.2 and 2.8 V (inset of Figure S6 in Supporting Information) when the sample is charged at 4.5 V, which could indicate a small fraction of cations (Ni or W) in different coordination environments. More importantly, it clearly appears that the irreversible capacity in the first cycle is due to the redox process at 4.2 V.

Ex situ samples were prepared along the first two cycles, and their XRD patterns were measured to look for structural changes during cycling (Figure 7b). In addition to significant broadening of the peaks, a reversible shift of the peak positions is observed upon charge and discharge. Superstructure peaks are preserved, suggesting that the W ordering is not affected, and all patterns can be indexed with the same *Cm* space group as the pristine material using the LeBail method, with the refined lattice parameters shown in Figure 7a and listed in Table S8 in Supporting Information. At 4 V, the slight decrease in in-plane lattice parameters *a* and *b* and increase in out-of-plane parameter *c* are consistent with the contraction of the honeycomb layer containing the majority of Ni (layer 1 in Figure 2) upon Ni oxidation and removal of $Li^+$ from the interlayer space. When charged further, all parameters decrease, with a large jump between 4.5 and 5 V, leading to a total contraction of the unit cell volume of 7%. The cell size increases back to close to its initial value on the next discharge, with slight differences in cell parameters that reflect the nonreversibility of the redox process at 4.2 V on initial charging. A similar evolution is observed in the second cycle with a less pronounced contraction at 5 V. Surprisingly, the most drastic volume change happens between 4.5 and 5 V on charge and between 5 and 3 V on discharge, whereas this corresponds to less than $0.5Li^+$ (de)inserted from the material, suggesting that another structural process participates in the substantial contraction of the unit cell.

**Charge Compensation Mechanism.** The high initial charge capacity (270 mAh/g) and reversible discharge capacity (200 mAh/g) cannot be explained solely by the $Ni^{2+}/Ni^{4+}$ redox couple, which can only provide up to 116 mAh/g on the first cycle (Ni is partially oxidized in the pristine $Li_{4.15}Ni^{3+}{}_{0.15}Ni^{2+}{}_{0.7}WO_6$) and 127 mAh/g on the next cycles. To understand the role played by Ni, W, and O in the different electrochemical processes, we measured selected ex situ samples by several spectroscopic techniques. X-ray absorption spectros-



DOI: 10.1021/jacs.8b13633
J. Am. Chem. Soc. 2019, 141, 7333−7346

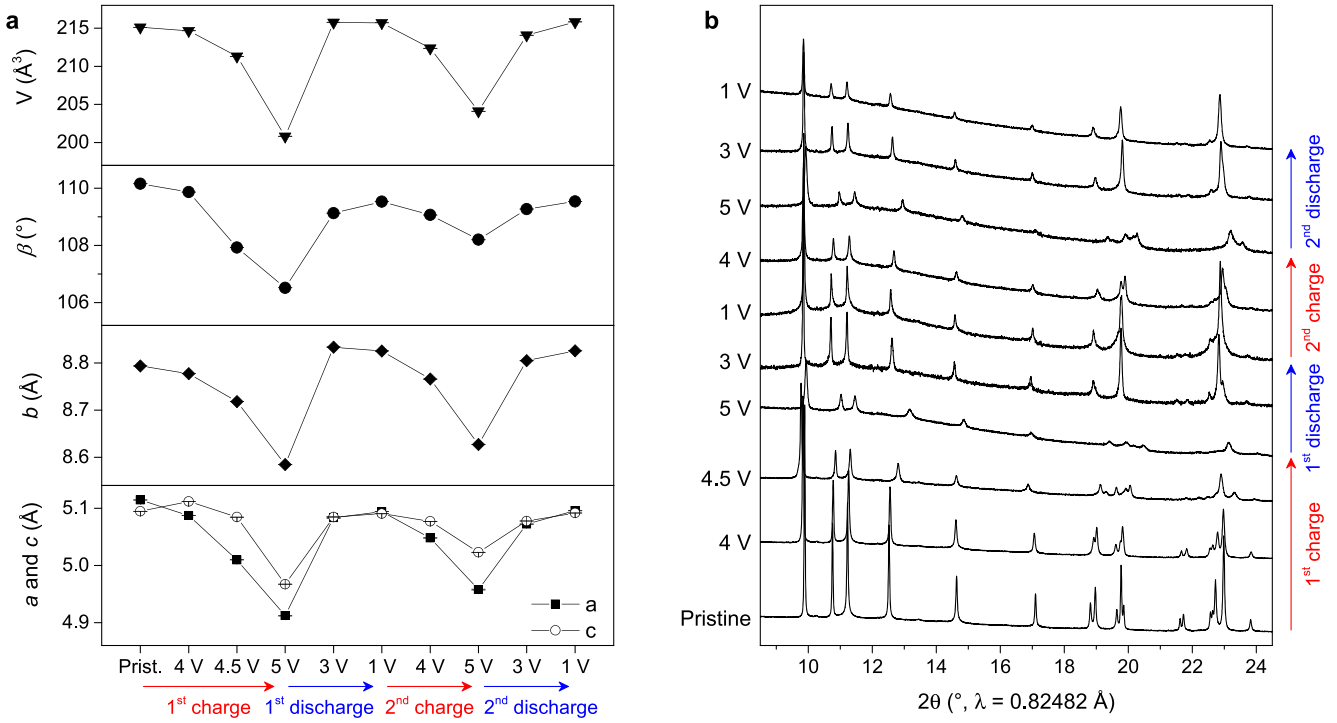


**Figure 7.** Ex situ X-ray diffraction study of $Li_{4.15}Ni_{0.85}WO_6$ for the first two cycles. (a) Evolution of cell parameters from pattern matching using the *Cm* space group of the pristine material. The unit cell contracts by 7% upon the first full charge and 5% on the second charge, suggesting an important modification of interatomic distances at high voltage. (b) Diffraction patterns at different states of the charge and discharge cycles. The conservation of superstructure peaks between 10 and 18° confirms that the honeycomb ordering of W cations is preserved upon cycling.

copy at the W $L_3$-edge (Figure 8a) shows a very slight change in shape of the absorption peak from 4 to 4.5 V that cannot be assigned to a change of oxidation state but rather to a distortion of the W local environment. This is consistent with an irreversible transformation of the material associated with the 4.2 V process, as the double peak initially observed seems to coalesce and remains unchanged on further cycling. The Ni K-edge was used to probe the activity of Ni, with $NiWO_4$ and $LiNiO_2$ as standards for +2 and +3 oxidation states, respectively. The edge position of the pristine sample is similar to that of the $NiWO_4$ standard (Figure 8b), as expected on the basis of the predominance of the $Ni^{2+}$ oxidation state in the starting material. Upon charging to 4 V, the edge gradually shifts to higher energies and finally reaches the edge position of the $LiNiO_2$ standard at 4.5 V, indicating the oxidation of $Ni^{2+}$ to $Ni^{3+}$. Slight changes can be more easily visualized by plotting the difference between two successive spectra (Figure S7 in Supporting Information). Further oxidation to 5 V does not affect the edge, which suggests that the Ni oxidation is limited to $Ni^{3+}$, making $Li_{4.15}Ni_{0.85}WO_6$ a rare example of a cathode material where the average oxidation state of nickel is considerably less than +4 after charging to 5 V. This limitation cannot be attributed to reduced sensitivity of the Ni K-edge to oxidation states higher than 3+ as several studies have shown a clear shift between trivalent and quadrivalent nickel compounds,[28,29] including an in situ study of the $Li_{1-z}Ni_{1+z}O_2$ ($z \leq 0.02$) cathode.[30] On discharge, Ni is partially reduced back to an oxidation state between $Ni^{2+}$ and $Ni^{3+}$ at 3 V and to $Ni^{2+}$ when discharged to 1 V. During the second cycle, the oxidation of Ni seems to start at a higher voltage, between 4 and 4.5 V (Figure 8c), but does not reach the full $Ni^{3+}$ oxidation state. This is possibly a consequence of structural reorganization during the first cycle that leaves some $Ni^{2+}$ ions inactive in the material, resulting in a broadening of the Ni K-edge maximum but no clear shifts of the edge position.

At this point, it is very surprising that only the $Ni^{2+}/Ni^{3+}$ redox couple is active in the material because it should theoretically account for about 64 mAh/g whereas the reversible capacity reaches 200 mAh/g, leaving two-thirds of the capacity unexplained. To investigate the possible participation of oxygen redox in the charge compensation mechanism, O 1s XPS spectra were collected to probe the presence of oxidized oxygen species. Figure 9b compares the XPS results for samples charged and discharged at different voltages on the first cycle. Up to 4.5 V, the spectra are dominated by the signal of oxygen $O^{2-}$ at 530.6 eV and show little variation, with only a weak contribution at higher binding energy for 4 and 4.5 V. This feature appears very clearly for the sample charged at 5 V as an intense contribution at higher binding energy (532.2 eV), which can be explained by the formation of oxidized oxygen species, written as $O^{n-}$ ($0 \leq n < 2$), until more information about their chemical nature is obtained as discussed below. Other contributions arising from deposited species are also very intense for this sample (~ 534 eV) because we expect some electrolyte decomposition at the cathode surface at high voltage. Upon discharge, the relative intensity of the $O^{n-}$ peak decreases compared to that of the $O^{2-}$ one but does not fully disappear, suggesting that some of the $O^{n-}$ species formed are not reduced back to oxide. In the second cycle (Figure S8 in Supporting Information), the contribution at 532.2 eV increases again at 4.5 V, a lower voltage compared to that in the first cycle. The same observations can be made by monitoring the W 4f doublet position, which is very sensitive to changes in the local environment of W ions (Figure 9b). At 5 V, the doublet shifts to higher binding energy, suggesting an increase in the ionicity of W−O bonds with decreasing Li



DOI: 10.1021/jacs.8b13633
J. Am. Chem. Soc. 2019, 141, 7333−7346

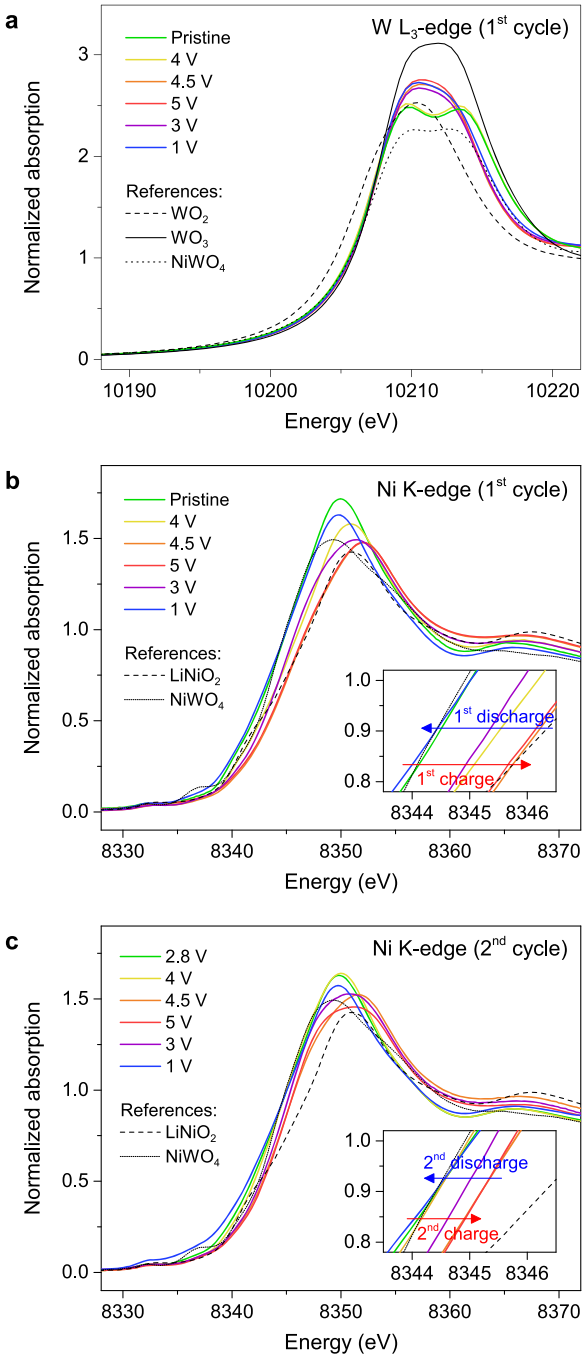


**Figure 8.** X-ray absorption spectroscopy data of cycled $Li_{4.15}Ni_{0.85}WO_6$. Ex situ spectra at the W $L_3$-edge on the first cycle (a) and the Ni K-edge on the first (b) and second (c) cycles were measured for cycled samples at different states of charge/discharge. The spectra for $W^{4+}O_2$, $W^{6+}O_3$, $Ni^{2+}W^{6+}O_4$, and $LiNi^{3+}O_2$ are given as references.

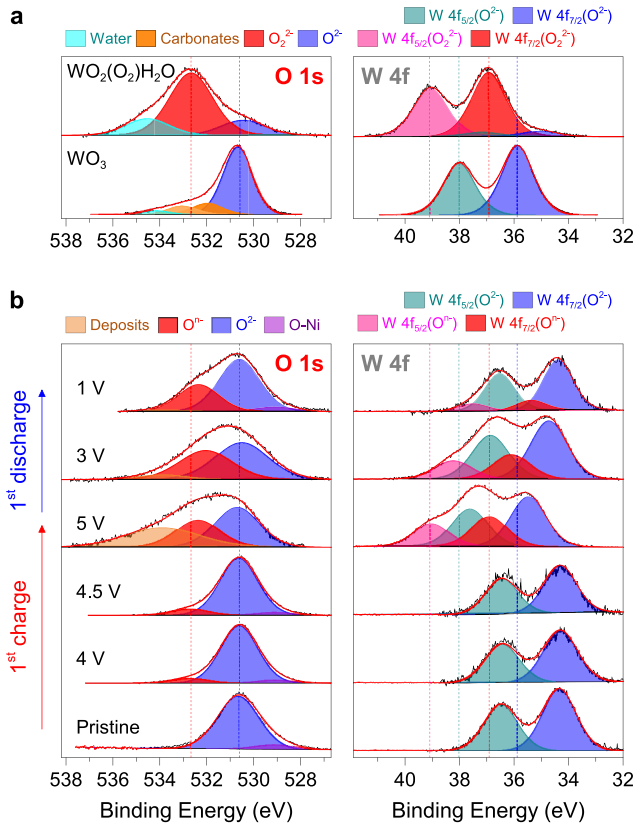


**Figure 9.** O 1s and W 4f X-ray photoemission spectroscopy data collected on standard W compounds (a) and during the first charge/discharge cycle of $Li_{4.15}Ni_{0.85}WO_6$ (b). The black and red lines are the experimental points and the result of the fit, respectively. In the O 1s spectra, the contributions of $O^{2-}$ and $O^{n-}$ (or $(O_2)^{2-}$ for $WO_2(O_2)$-$H_2O$) are shown in blue and red, respectively. Surface deposits from decomposition products of the carbonate-based electrolyte are in orange, and a small contribution at lower binding energy that we attribute to an oxygen environment rich in nickel is shown in purple. A contribution of water is also shown in cyan for $WO_2(O_2)H_2O$. The W 4f doublet is shown in blue ($4f_{7/2}$) and dark cyan ($4f_{5/2}$) for the contribution with a nonoxidized oxygen environment and in red ($4f_{7/2}$) and pink ($4f_{5/2}$) for the contribution with oxidized oxygen $O^{n-}$. Dashed line are guides for comparing the positions of the different peaks to those in the standard samples.

content, and a new doublet appears, whose evolution closely follows that of the $O^{n-}$ peak in the O 1s spectra. This new doublet is therefore assigned to a new W environment coordinated by the oxidized $O^{n-}$ species, and its relative intensity is correlated with the amount of oxidized oxygen next to the surface of the sample. To strengthen this assignment, we measured the XPS spectra of two reference samples with $W^{6+}$ cations in different coordination environments, namely, $WO_3$ and $WO_2(O_2)H_2O$,[31] the latter containing a peroxo $(O_2)^{2-}$ ligand (Figure 9a). The positions of the O 1s peak (530.7 eV) and W 4f doublet (35.9−38.0 eV) of $WO_3$ are in good agreement with the corresponding $O^{2-}$ (530.7 eV) and W-($O^{2-}$) (35.5−37.6 eV) peaks of the fully charged sample, whereas the positions of the O 1s peak (532.7 eV) and W 4f doublet (36.9−39.0 eV) of $WO_2(O_2)H_2O$ correspond to the $O^{n-}$ (532.4 eV) and W-($O^{n-}$) (36.9−39.0 eV) peaks in the fully charged sample. Finally, the 2.14 eV splitting of both W-($O^{2-}$) and W-($O^{n-}$) doublets remains constant at any state of charge, confirming that W is in the +6 oxidation state at all points along the charge/discharge curves. It is quite unexpected that most oxidized oxygen species appear above 4.5 V on the first charge, whereas Ni does not oxidize beyond +3 according to XAS, leaving a gap in our understanding of the charge compensation mechanism between OCV and 4.5 V. Because XPS is a surface-sensitive technique and mostly probes the first 5 nm below the surface, it is possible that oxygen is oxidized at lower potential in the bulk of the material, as is suggested by the low-intensity



DOI: 10.1021/jacs.8b13633
J. Am. Chem. Soc. 2019, 141, 7333−7346

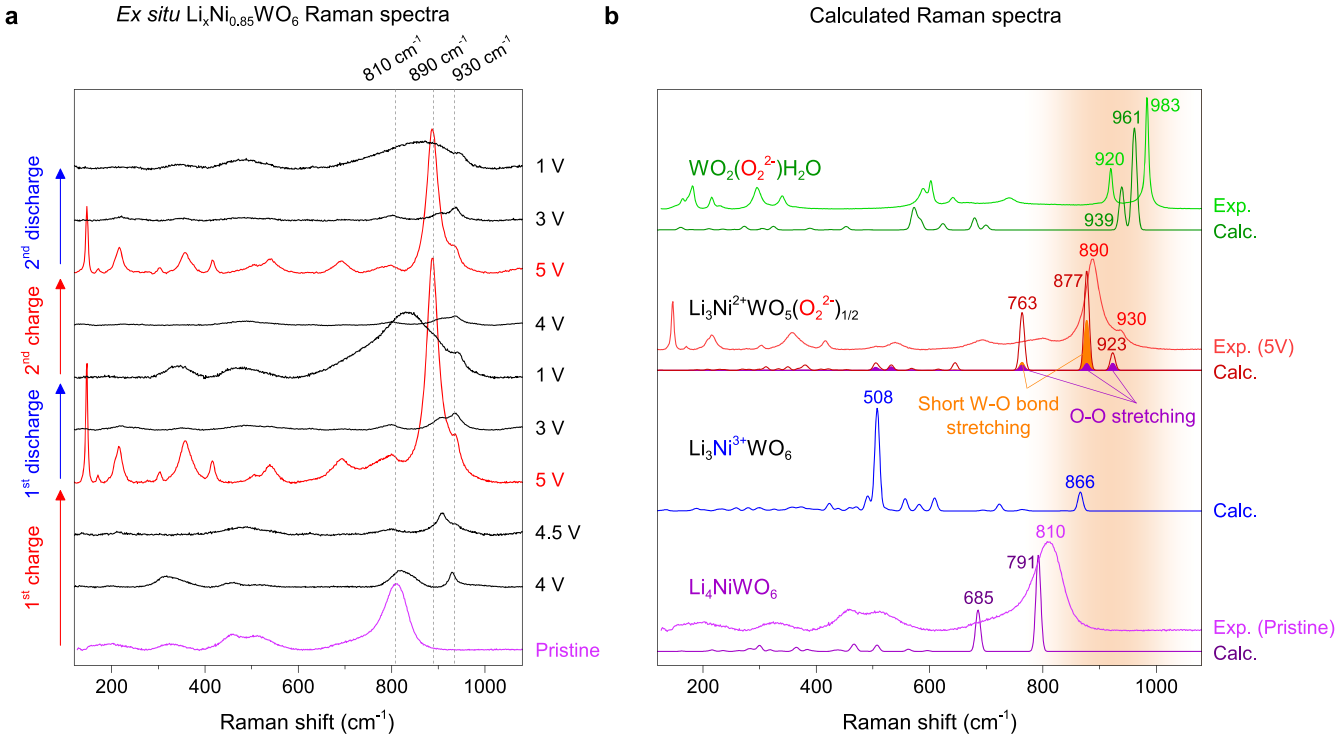


**Figure 10.** Experimental and calculated Raman spectra. (a) Ex situ Raman spectra for different states of charge/discharge of $Li_{4.15}Ni_{0.85}WO_6$. The pristine and fully charged spectra are highlighted in light purple and red, respectively. (b) Calculated Raman spectra for the pristine $Li_4NiWO_6$ (purple), two models of delithiation assuming cationic ($Li_3Ni^{3+}WO_6$, blue) and anionic redox ($Li_3Ni^{2+}WO_5(O_2^{2-})_{1/2}$, red), and the reference sample $WO_2(O_2)H_2O$ (green). Experimental spectra of the pristine material (light purple), charged to 5 V (light red), and $WO_2(O_2)H_2O$ (light green) are also plotted for comparison with the calculated ones. The typical range of frequencies for the peroxide O−O stretching mode is shaded in the figure from 800 to 1000 $cm^{-1}$.

contribution in the 4 and 4.5 V samples consistent with the $O^{n-}$ peak at 532.2 eV, whereas the oxygen species oxidized close to the surface evolve as oxygen gas and are therefore not observed.

**Formation of Stable O−O Bonds.** If anionic redox can explain the high reversible capacity of $Li_{4.15}Ni_{0.85}WO_6$ (200 mAh/g on first cycle) despite the minor participation of Ni in the charge compensation mechanism, the low voltage of the reduction plateau at 1.7 V highlights the difficulty in reducing the oxidized $O^{n-}$ species formed during charging. Because of its $d^0$ electronic configuration and associated $\pi$-acceptor character, $W^{6+}$ is prone to stabilize peroxo $(O_2)^{2-}$ ligands in aqueous media through the formation of coordination complexes,[32] similarly to other $d^0$ transition metal species such as $Ti^{4+}$. $WO_2(O_2)H_2O$ is such an example, with an O−O bond of 1.46 Å, and shows clear signature peaks between 900 and 1000 $cm^{-1}$ in both infrared[31] and Raman spectroscopy (light green in Figure 10b). The most intense peak at 983 $cm^{-1}$ is generally assigned to the short W−O bond stretching mode,[33] and the less intense peak at 920 $cm^{-1}$ is assigned to the stretching of the peroxo O−O bond. Computed Raman spectra (dark green) using DFT calculations can fairly well reproduce these two features (961 and 939 $cm^{-1}$, respectively) and further demonstrate that both peaks correspond to combinations of stretches of the short W−O and peroxo O−O bonds. This result shows that the presence of a peroxo bond does not necessarily result in one but possibly several vibrational modes, which is the case for $Na_2O_2$, $MgO_2$, and $ZnO_2$,[34] and that the DFT calculation can provide decisive insight for the correct assignment of the Raman peaks.

To check the formation of O−O bonds in the bulk structure of $Li_xNi_{0.85}WO_6$, we recorded Raman spectra of ex situ samples at different states of charge (Figure 10a) and compared them to those obtained by DFT calculations on two model systems $Li_3Ni^{3+}WO_6$ and $Li_3Ni^{2+}WO_5(O_2^{2-})_{1/2}$ with delithiation mediated by Ni redox and O redox, respectively (Note 4 and Figure S9 in Supporting Information). The pristine material has one main broad Raman band at 810 $cm^{-1}$ corresponding to the W−O stretching mode and less intense peaks (327, 460, 515 $cm^{-1}$) at lower frequency, where one expects bending and deformation modes. Upon charging to 4 V, the intensity of the main peak decreases and a sharper peak appears at 930 $cm^{-1}$, joined by a second peak at 910 $cm^{-1}$ at 4.5 V. Finally, the fully charged sample (5 V) shows a very well defined Raman spectrum, with relatively sharp and intense peaks, suggesting that the local structure of the fully charged sample is fairly ordered. Focusing on the peaks in the 800−1000 $cm^{-1}$ region in the fully charged sample, we observe a very intense peak at 890 $cm^{-1}$ and a second peak at 930 $cm^{-1}$ that appears as a shoulder. The peak at 930 $cm^{-1}$ is then present in all subsequent spectra, including the fully discharged samples, whereas the most intense band progressively disappears again upon discharge and is replaced at 1 V by a broader band centered at 830 $cm^{-1}$. In the second cycle, a perfectly reversible evolution is observed, consistent with the improved electrochemical reversibility after the first cycle. The position of the peak at 930 $cm^{-1}$ is in excellent agreement with that at 920 $cm^{-1}$ in $WO_2(O_2)H_2O$ and could result from the formation of a peroxo bond. Calculation of the Raman modes was therefore performed with DFT to confirm



DOI: 10.1021/jacs.8b13633
J. Am. Chem. Soc. 2019, 141, 7333−7346

the assignment of the peaks, using the pristine structure and two models of delithiation mediated by Ni redox (blue spectra in Figure 10b) and O redox (red spectra) respectively, the latter being characterized by the formation of a peroxo $(O_2)^{2-}$ unit ($d_{O-O}$ = 1.46 Å, Figure S10 in Supporting Information). The calculated spectra are shown in Figure 10b, with the contributions of the short W−O and O−O vibrations to the different peaks of the peroxo-containing model highlighted in orange and purple, respectively. It is important to note that the O−O vibration resulting from peroxide formation in the $Li_3Ni^{2+}WO_5(O_2^{2-})_{1/2}$ model is again not associated with just one but several vibrational modes, including the most intense peak at 877 $cm^{-1}$, which has a major contribution from the short W−O stretching mode and a smaller contribution from the peroxide O−O stretch along with a smaller peak at 923 $cm^{-1}$, where the main component is the peroxide O−O stretch. These two peaks predicted by the DFT model are in excellent agreement with the intense peak (890 $cm^{-1}$) and shoulder (930 $cm^{-1}$) observed experimentally in the fully charged sample. The model also shows some contribution of the peroxide to the vibrational mode at 763 $cm^{-1}$ and we do measure a small peak in the experimental spectra, but this mode mainly corresponds to W−O−Ni vibrations and is therefore less intense in the material with partial Ni disorder compared to the ordered DFT model. If the $Li_3Ni^{2+}WO_5(O_2^{2-})_{1/2}$ model does not perfectly represent the structure of the material charged at 5 V, then it does capture the effect of forming a peroxo bond on the calculated Raman spectra. By comparison, the model with the oxidation of nickel results in a single peak above 800 $cm^{-1}$ which is inconsistent with the experimental observations. The observed values for O−O stretching frequencies (880−930 $cm^{-1}$) are higher than the Raman signals previously reported for in situ Raman studies of $Li_{1.2}Ni_{0.2}Mn_{0.6}O_2$ and $Na_3RuO_4$ (850 $cm^{-1}$),[35,36] a difference that could arise from the use of isolated gold nanoparticles to enhance the Raman signal of the first 1−5 nm of the sample's surface. In the case of ex situ Raman measurements, depths of 100 nm to a few micrometers are probed depending on the materials,[37] making it bulk-sensitive. Raman spectroscopy and surface enhanced Raman spectroscopy (SERS) studies have shown different results on the same $Li(Li_{0.2}Ni_{0.2}Mn_{0.6})O_2$ material,[35,38] highlighting that different processes can happen at the surface and in the bulk of the particles. The frequencies we find are closer to the frequencies encountered for $MgO_2$ (864 and 934 $cm^{-1}$) and $ZnO_2$ (847 and 944 $cm^{-1}$) compared to those of $Li_2O_2$ (790 $cm^{-1}$) and $Na_2O_2$ (736 and 791 $cm^{-1}$).[34] Such differences are likely to arise from different O−O bond orders, which may greatly vary depending on the metal center: here we emphasize the role of $W^{6+}$ in coordinatively stabilizing the peroxide species. The agreement between experimental and calculated Raman spectra, and more importantly the comparison with the structurally and spectroscopically well-defined hydrated tungsten peroxide $WO_2(O_2)H_2O$, provides strong evidence for the formation of localized peroxo oxygen−oxygen single bonds upon full charge of $Li_{4.15}Ni_{0.85}WO_6$. This is consistent with the oxidized oxygen signal obtained from XPS, which also agrees with measurements on the same peroxide-containing $WO_2(O_2)H_2O$ standard, and shows that the redox of oxygen is not only happening at the surface but is indeed a bulk effect. The formation of quasi-molecular $(O_2)^{2-}$ species explains the shift of the W 4f doublet at higher binding energy (Figure 9b) with the increased ionicity of W-$(O_2)^{2-}$ bonds compared to W−$O^{2-}$ bonds. This can also explain the strong contraction of the unit cell observed by diffraction at the end of charge (Figure 7a) in which the formation of peroxo bonds would be expected to strongly perturb interatomic distances in the material. Finally, the fact that the peak at 930 $cm^{-1}$ does not completely disappear at the end of the first cycle is also consistent with the XPS data and indicates that some peroxo species are formed irreversibly and maintained through subsequent cycling, thus explaining some of the irreversible capacity of the first cycle.

## DISCUSSION

By combining different techniques, we have obtained some insights into the electrochemical behavior of $Li_{4.15}Ni_{0.85}WO_6$. One of the most surprising results is the impossibility of accessing the $Ni^{3+}/Ni^{4+}$ redox, which suggests close competition between the redox activities of Ni and O. This results stands out from the behavior of the related $Li_4NiTeO_6$, which uses the full $Ni^{2+}/Ni^{4+}$ redox couple with less than 200 mV hysteresis between charge and discharge.[22] Moving from a main group cation ($Te^{6+}$) to a $d^0$ cation ($Mo^{6+}$, $W^{6+}$) as non-redox-active elements not only affects the cation ordering in the structure but also drastically changes the electrochemical properties of the material. Here, the activation of redox of oxygen-based states is demonstrated by the alignment of both Raman and XPS spectra of electrochemically delithiated samples with tungsten peroxide standard $WO_2(O_2)H_2O$. DFT calculations were carried out to investigate the electronic structure of delithiated $Li_4NiWO_6$ using both the VASP PBE+U and HSE06 total energies. (See Note 4 in SI for details on the calculation.) An idealized cation-ordered $Li_4NiWO_6$ structure was used for the calculations, with the experimental tungsten positions fixed and Ni/Li ordering with the lowest-energy configuration. The two models of delithiation previously described were then explored (Figure S11 in Supporting Information), mediated by Ni redox and O redox, respectively. The computed voltage for $x$ = 1 in $Li_{4-x}NiWO_6$ is found to be 0.2−0.4 V higher for the anionic redox than for the cationic $Ni^{2+}/Ni^{3+}$ model (Table S9 in Supporting Information), which is consistent with our observation of Ni oxidation at 3.7 V, and highlights the small difference in energy between cationic and anionic redox in this material. The stabilization of peroxide upon further oxidation could prevent the activation of the $Ni^{3+}/Ni^{4+}$ redox couple or else could be mediated by removing electrons from Ni $e_g$ states to form transient $Ni^{4+}$ species, according to the reductive coupling mechanism proposed for Ru-based materials.[1,39] However, no change in the oxidation state of Ni beyond 3+ is observed experimentally, so this second hypothesis cannot be confirmed. Because irreversibility increases when charging above 4 V, the material probably undergoes some irreversible oxidation of oxygen and gas release from the surface, corresponding to the process at 4.2 V on the first charge. This would explain why oxidized oxygen species are not observed by XPS in ex situ samples until 5 V. Nevertheless, the reversible formation of peroxo $(O_2)^{2-}$ species in the second cycle, measured by Raman and XPS, proves that the large reversible capacity on discharge (200 mAh/g) is due to both cationic and anionic redox, contributing respectively to one-third and two-thirds of the capacity. If we assume that the $Ni^{2+}/Ni^{3+}$ redox is fully used, then 1.75$e^-$ are to be accounted for by oxygen (i.e., 0.29$e^-$/O after normalizing by the number of oxygen in the formula unit), which is 16% higher than in Li-rich NMC (0.25$e^-$/O) according to Luo et al.,[40] reflecting the possibility of attaining considerable reversible anionic redox capacity from localized O−O bond formation.


DOI: 10.1021/jacs.8b13633
J. Am. Chem. Soc. 2019, 141, 7333−7346

Turning to the large voltage hysteresis observed upon activation of oxygen redox, it should be underlined that this is a true concern for the development of Li-rich cathode materials[41] because it results in a large penalty in the round-trip energy efficiency (<90% for Li-rich NMC). Such hysteresis has been correlated with oxygen redox activity and cationic migrations,[13,15,42] which both result in different thermodynamic pathways on charge and discharge. One pending question is how the choice of a transition metal affects the bond order and reversibility of O−O bond formation upon charge and discharge. The use of high-valence $d^0$ cations to increase the lithium content leads to higher capacities, thanks to the combined participation of cationic and anionic redox. However, the XPS and Raman evidence on $Li_{4.15}Ni_{0.85}WO_6$ suggests that high-valence $d^0$ cations also stabilize the formation of localized O−O bonds with a bond order $n$ close to 1, which results in a large energy penalty associated with breaking the bonds upon reduction. It is well illustrated by density of states calculations that the empty antibonding ($\sigma^*$) states of quasi-molecular $(O_2)^{2-}$ species in the model derived from $Li_4NiWO_6$ by the oxidation of oxygen are difficult to reduce back because they lie well above the Fermi level (Figure S11c in Supporting Information). Such a reduction is possible in $Li_{4.15}Ni_{0.85}WO_6$ at a very low discharge voltage of 1.7 V that makes the energy efficiency drop dramatically to 50%. The same redox processes are observed in the stoichiometric $Li_4NiWO_6$ (Figure S5 in Supporting Information), showing that the presence of isolated $WO_6$ octahedra is enough to stabilize $(O_2)^{2-}$ species whereas the long-range cation ordering does not impact the electrochemical behavior. The local coordination of oxygen atoms is comparable in both materials with every oxygen coordinated by one W cation as well as one Ni and four Li cations on average, although the imperfect ordering of Ni/Li will also result in other local coordination configurations around oxygen and a distribution of environments for Ni and Li which could explain why we do not see well-defined delithiation steps. Both materials also offer high-dimensional diffusion pathways for Li diffusion. Similar voltage hysteresis has been observed in disordered rock salt $Li_{1.2}Ni_{1/3}Ti_{1/3}Mo_{2/15}O_2$[43] as well as in the $Li_4NiMoO_6$ phase reported by Yabuuchi et al.,[12] suggesting that a stabilization of O−O bonds by $d^0$ cations could be present in these materials as well and inviting further characterization by Raman spectroscopy. In the present case, the Raman spectra demonstrate the role of the redox-inactive $W^{6+}$ cation in stabilizing peroxides through coordinative interactions, distinct from other species potentially involved in redox processes (holes on oxygen $O^{n-}$, peroxo-like $(O_2)^{n-}$, superoxide $(O_2)^-$, and gaseous $O_2$). Among all cathode materials showing anionic redox, those containing late 4d/5d transition metals such as Ru/Ir form O−O pairs with much lower bond order ($d_{O-O} \approx 2.4$ Å) and almost certainly differing extents of oxygen hole localization compared to that of the $3d^n/5d^0$ system studied here. This would lead to less destabilized antibonding $\sigma^*$ states, thus improving the reversibility of the process and resulting in relatively low voltage hysteresis because of the reduced energy penalty for occupying these less-antibonding states.[26,39,44] To take full advantage of the high capacity of $d^0$-based Li-rich rock salt oxides, one needs to facilitate the reduction of the O−O bonds. This could be done by stabilizing intermediate O−O distances ($1.4 < d_{O-O} < 2.4$ Å) through optimization of the extent of delocalization of charges over the oxygen atoms in the structure or lowering the barrier to electron transfer into the antibonding states. Both of these scenarios are likely to be achieved by a careful selection of cations to minimize hysteresis and maximize the anion redox capacity accessible from the formation of O−O bonds (i.e., by optimizing the extent of localization of the oxygen holes).

## CONCLUSIONS

In this work, the structural and electrochemical properties of a family of Li-rich rock salt oxides $Li_{4+x}Ni_{1-x}WO_6$ were explored. The cation ordering is very sensitive to the Li/Ni ratio and generates two new structure types derived from $Li_3Ni_2TaO_6$ for Li/Ni = 4 and $Li_5ReO_6$ for Li/Ni > 4. Similar electrochemical processes were found regardless of the cation ordering, but a higher reversible capacity was measured for the $Li_{4.15}Ni_{0.85}WO_6$ sample compared to the stoichiometric one. Surprisingly, Ni could not be oxidized beyond $Ni^{3+}$ even at high voltage (5 V), accounting for only 64 mAh/g (i.e., one-third of the total reversible capacity (200 mAh/g)), thus leaving the large reversible capacity mostly unexplained by a classical cationic redox mechanism. The capacity associated with oxygen redox in this material is thus considerably larger than that obtained from the oxidation of the $3d^n$ cations. Raman spectroscopy combined with DFT calculation on the cycled material and a known tungsten peroxide standard compound represents definitive evidence of the formation of true peroxo $(O_2)^{2-}$ anions with localized O−O single bonds, stabilized by the presence of $5d^0$ $W^{6+}$ cations consistent with the solution coordination chemistry of $d^0$ peroxo complexes. This results in good reversibility of the anionic redox process after the first activation cycle, with a very large voltage hysteresis between charge and discharge that we attribute to the difficulty in reducing the stabilized $(O_2)^{2-}$ species, highlighting the importance of balancing electrochemical access to oxygen oxidation with enabling its reversal. The electronic structure and bonding characteristics of both redox-active (Ni) and redox-inactive (W) components of the structure play key roles in controlling the capacity accessible by stabilizing localized O−O bonds and the reversibility of the bond formation that defines the efficiency of the energy storage process. Such findings can be generalized to other $d^0$-containing Li-rich rock salt oxides, which also struggle with large voltage hysteresis and low energy efficiency, although the origin of this issue had not been investigated until now. Having clarified this point, we expect that this work will help in defining new strategies to decrease the voltage hysteresis and bring high-capacity rock salt oxides closer to potential applications.

## METHODS

**Synthesis.** Pale-green powder samples of $Li_4NiWO_6$ were prepared by a conventional ceramic route. A stoichiometric mixture of $Li_2CO_3$ (99.997%, Sigma-Aldrich, dried at 250 °C for 12 h), NiO (99.999%, Sigma-Aldrich, dried at 250 °C for 12 h), and $WO_3$ (99.995%, Sigma-Aldrich, dried at 250 °C for 12 h) was ball-milled in propanol for 2 h, dried, pressed into a pellet, and loaded into an alumina crucible to produce ~1 g of material. Part of the precursor mixture was used as a sacrificial powder in order to minimize the effects of Li volatility. The samples were fired twice at 1000 °C for 24 h with a heating/cooling rate of 5 °C/min, with intermediate hand grinding of the pellet and sacrificial powder between firings. Brown-black powder samples of $Li_{4+x}Ni_{1-x}WO_6$ ($0 \le x \le 0.25$) were prepared as above but with a 10% molar excess of lithium in the appropriate ratio of starting materials (e.g., Li/Ni/W = 4.51:0.9:1 for $x = 0.1$). For the neutron powder diffraction (NPD) experiments, both $Li_4NiWO_6$ and $Li_{4.1}Ni_{0.9}WO_6$ were enriched with $^7Li$ using $^7Li_2CO_3$ (99% $^7Li$ atom, Sigma-Aldrich dried at 250 °C for 12 h), with the synthesis scaled up to 4 g of product. $WO_2(O_2)H_2O{\cdot}nH_2O$ was prepared following the method described by



DOI: 10.1021/jacs.8b13633
J. Am. Chem. Soc. 2019, 141, 7333−7346

Pecquenard et al.,[31] followed by a thermal treatment at 120 °C for 12 h to prepare reference sample $WO_2(O_2)H_2O$.

**Diffraction.** Phase identification of the $Li_{4+x}Ni_{1-x}WO_6$ samples was conducted using laboratory powder X-ray diffraction data obtained using a PANalytical X'Pert Pro diffractometer (Co K$\alpha_1$) in Bragg–Brentano geometry. This instrument was also used for the determination of lattice parameters in the $Li_{4+x}Ni_{1-x}WO_6$ ($0 \le x \le 0.25$) series by the inclusion of crystalline Si as an internal standard. For detailed structural analysis of the as-synthesized materials, synchrotron X-ray powder diffraction (SXRD) data were collected at the I11 beamline at the Diamond Light Source (Oxfordshire, U.K.), with an incident wavelength of 0.82588(1) Å using five multianalyzer crystal detectors. The samples were loaded into borosilicate capillaries of 0.1 mm diameter to minimize the absorption cross-section of the sample and mounted on a capillary spinner during data collection. High-resolution time-of-flight (ToF) neutron powder diffraction (NPD) data were collected at room temperature using the HRPD instrument at ISIS (Oxfordshire, U.K.). The structural models were refined by the Rietveld method[45,46] using the TOPAS software.

**Electrochemical Testing.** To evaluate the performance of $Li_{4+x}Ni_{1-x}WO_6$ ($x$ = 0.15) as a Li-ion battery cathode material, composite electrodes were fabricated by casting a mixture of active material/Super C carbon/poly(vinylidene fluoride) (PVDF) binder (Kynarflex, Arkema) (80:10:10 by wt) onto an aluminum foil current collector. Coin cells (CR2025) were assembled in an argon-filled glovebox using 1 M $LiPF_6$ in ethylene carbonate/dimethyl carbonate (BASF) 1:1 by volume as the electrolyte, impregnated onto a glass fiber separator (Whatman) with a lithium metal counter electrode. Electrochemical characterization was carried out with a Maccor Series 4000 battery cycler, at 25 °C, using a C rate of C/10 (defined as 1 $Li^+$ exchanged in 10 h) between 1 and 5 V. For the preparation of ex situ samples, electrodes were cycled to different charge/discharge states, recovered, washed with DMC in the glovebox, and dried.

**Ex Situ PXRD of Charged Cathodes.** Samples mixed with Super C carbon (80:20 by wt) were cycled to different states of charge/discharge in Swagelok cells. They were recovered, washed with DMC, and dried under vacuum before being loaded into borosilicate tubes (0.3 mm diameter). The capillaries were sealed with wax prior to removal from the glovebox and then heat sealed with a blowtorch. PXRD of the samples was collected at the I11 beamline with an incident wavelength of 0.826212 Å using a wide-angle position-sensitive detector.

**X-ray Absorption Spectroscopy (XAS).** The X-ray absorption spectra were recorded at the B18 beamline at the Diamond Light Source (Oxfordshire, U.K.). X-ray absorption near-edge structure (XANES) spectroscopy was used for the analysis of the nickel and tungsten oxidation states, near the Ni K- and W $L_{III}$-edges. The data was calibrated using Ni/W metal foil references and normalized with the Athena software.[47] Electrodes for ex situ XAS were prepared by pressing a pellet (~60 mg) of active material with super C carbon and PVDF binder (74:13:13 by wt). After washing the samples, the active electrode pellets were mixed with an appropriate amount of cellulose (Sigma-Aldrich), pressed to the appropriate density, and sealed into polyethylene-lined foil bags (Sigma-Aldrich) to prevent air exposure. Samples of uncycled active material were prepared in an analogous way, including the carbon and binder. Materials used as reference standards including $NiWO_4$ ($Ni^{2+}$ and $W^{6+}$ standard), $WO_3$ ($W^{6+}$ standard), and $WO_2$ ($W^{4+}$ standard) were prepared by mixing appropriate masses of each with cellulose and pressed as pellets but were not sealed in polyethylene foil bags.

**X-ray Photoelectron Spectroscopy (XPS).** Measurements were performed in a standard ultrahigh vacuum surface science chamber consisting of a PSP Vacuum Technology electron energy analyzer (angle integration ±10°) and a dual-anode Mg K$\alpha$ (1253.6 eV) X-ray source. The base pressure of the system was $2 \times 10^{-10}$ mbar, with hydrogen as the main residual gas in the chamber. The spectrometer was calibrated using Au $4f_{7/2}$ at 83.9 eV. All spectra were calibrated by aligning the main peak in the O 1s region to that measured from the reference $WO_3$ compound at 530.6 eV. XPS spectra were fitted using Voigt functions (30% Gaussian/70% Lorentzian) after Shirley background removal. The analysis was performed with the minimum number of components required to explain the data. In the case of W 4f spectra, the relative intensities of the $4f_{5/2}$ and $4f_{7/2}$ peaks were constrained from the ratio found for the pristine spectra. Samples were transported from the glovebox to the instrument using a dedicated transfer chamber to avoid contact with air.

**Raman Spectroscopy.** Ex situ measurements were performed at different stages of galvanostatic cycling. To avoid oxygen and moisture contamination, an airtight Raman cell (ECC-Opto-STD, El-Cell, GmBH) was assembled inside an argon-filled glovebox. Raman spectra were collected with a 633 nm wavelength laser using a Raman system (Renishaw inVia Reflex) with a microscope focused through a 50× objective lens (Leica). The estimated power on the sample was 0.43 mW with 200 s exposure time and two accumulations. The baseline of the spectra was corrected for clarity.

**Computational Methods.** Plane-wave-based density functional theory (DFT) calculations were performed with VASP,[48] using the PBE functional[49] augmented by an on-site Hubbard correction (PBE+U) using a rotationally invariant scheme[50] with a $U_{eff}$ of 7 eV applied to the Ni 3d states. Core electrons were treated using the projected augmented wave approach,[51] with the Li 1s, Ni 2p, and W 5s and 5p semicore states treated as valence states. A 700 eV plane-wave cutoff energy was used for calculations of final structures and properties, with a 7 × 7 × 4 $k$-point grid. A 600 eV plane-wave cutoff and a reduced $k$-point grid of 5 × 5 × 3 were used when screening the energies of many configurations, which was sufficient to obtain relative energies within 20 meV of those obtained using the more accurate settings. In general, the unit cell and atomic positions of structures were optimized until all forces were below 0.01 eV/Å, with a tighter convergence of 0.001 eV/Å used for the equilibrium structures of normal mode calculations.

Raman spectra are computed using the vasp_raman.py code.[52] A full normal mode calculations was performed at the Γ point using finite differences with displacements of 0.01 Å and the harmonic approximation. Following this, the change in the macroscopic dielectric tensor for each mode was calculated using density functional perturbation theory and was used to compute the Raman activity of the mode. Projection operators were evaluated in reciprocal space for these calculations to provide a high-enough accuracy.

Hybrid DFT calculations were performed with a Gaussian basis set using CRYSTAL14.[53] The HSE06 functional[54] was used to obtain a better prediction of delithiation potentials. The pob-TZVP triple-$\zeta$ valence with polarization basis functions was used for Li, Ni, and O,[55] and a modified Hay–Wadt double-$\zeta$ basis set was used for W, which had previously been shown to perform well for $WO_3$.[56] A $k$-point grid of 7 × 7 × 4 was used for each model, and the unit cell and atomic positions were optimized until the forces were below 0.01 eV/Å.

## ■ ASSOCIATED CONTENT

### Supporting Information

The Supporting Information is available free of charge on the ACS Publications website at DOI: 10.1021/jacs.8b13633.

Composition/structure analysis and computational summary; structural parameters, evolution of cell parameters upon cycling, and the calculated delithiation potential; structural information, SEM images, differential capacity plots, XPS for the second cycle of $Li_{4.15}Ni_{0.85}WO_6$, and results for the calculated structure and associated DOS (PDF)

$Li_4NiWO_6$ (CSD 1884635) (CIF)

$Li_{4.1}Ni_{0.9}WO_6$ (CSD 1884637) (CIF)

## ■ AUTHOR INFORMATION


### Corresponding Author

*rossein@liverpool.ac.uk

### ORCID

Arnaud J. Perez: 0000-0003-1659-554X

José A. Coca-Clemente: 0000-0002-9475-1889




DOI: 10.1021/jacs.8b13633
J. Am. Chem. Soc. 2019, 141, 7333–7346

Filipe Braga: 0000-0002-4070-821X
Michael J. Pitcher: 0000-0003-2044-6774
Matthew S. Dyer: 0000-0002-4923-3003
John B. Claridge: 0000-0003-4849-6714
Laurence J. Hardwick: 0000-0001-8796-685X
Matthew J. Rosseinsky: 0000-0002-1910-2483

**Present Address**

[⊥]CIC Energigune, Alava Technology Park, Calle Albert Einstein 48, 01510 Miñano, Spain.

**Notes**

The authors declare no competing financial interest.

## ■ ACKNOWLEDGMENTS

This work was funded by the EPSRC under EP/N004884 and a studentship for Z.N.T. Author F.B. acknowledges funding from the Science without Borders Program, Ministério da Educação, Coordenação de Aperfeiçoamento de Pessoal de Nível Superior (CAPES) Brazil. N.E.D. acknowledges the Engineering and Physical Sciences Research Council (EPSRC) under grant number EP/K016954/1. Central facilities time was provided by the STFC at the Diamond Light Source and the ISIS spallation source. We thank Dr. C. Murray for assistance at beamline I11, Prof. Alan Chadwick and Dr. Gianntonio Cibin for assistance at beamline B18, and Dr. A. Gibbs and Dr. D. Fortes for assistance at HRPD. We acknowledge Dr. A. Hloskovsky (DESY Photon Science, Hamburg, Germany) for helpful discussions on high-energy XPS. M.J.R. is a Royal Society Research Professor.

## ■ REFERENCES

(1) Saubanère, M.; McCalla, E.; Tarascon, J.-M.; Doublet, M.-L. The Intriguing Question of Anionic Redox in High-Energy Density Cathodes for Li-Ion Batteries. *Energy Environ. Sci.* **2016**, *9* (3), 984−991.

(2) Seo, D.-H.; Lee, J.; Urban, A.; Malik, R.; Kang, S.; Ceder, G. The Structural and Chemical Origin of the Oxygen Redox Activity in Layered and Cation-Disordered Li-Excess Cathode Materials. *Nat. Chem.* **2016**, *8* (7), 692−697.

(3) Perez, A. J.; Jacquet, Q.; Batuk, D.; Iadecola, A.; Saubanère, M.; Rousse, G.; Larcher, D.; Vezin, H.; Doublet, M.-L.; Tarascon, J.-M. Approaching the Limits of Cationic and Anionic Electrochemical Activity with the Li-Rich Layered Rocksalt $Li_3IrO_4$. *Nat. Energy* **2017**, *2* (12), 954.

(4) Xie, Y.; Saubanère, M.; Doublet, M.-L. Requirements for Reversible Extra-Capacity in Li-Rich Layered Oxides for Li-Ion Batteries. *Energy Environ. Sci.* **2017**, *10* (1), 266−274.

(5) Kumar, V.; Bhardwaj, N.; Tomar, N.; Thakral, V.; Uma, S. Novel Lithium-Containing Honeycomb Structures. *Inorg. Chem.* **2012**, *51* (20), 10471−10473.

(6) Nalbandyan, V. B.; Avdeev, M.; Evstigneeva, M. A. Crystal Structure of $Li_4ZnTeO_6$ and Revision of $Li_3Cu_2SbO_6$. *J. Solid State Chem.* **2013**, *199*, 62−65.

(7) Gupta, A.; Kumar, V.; Uma, S. Interesting Cationic ($Li^+/Fe^{3+}/Te^{6+}$) Variations in New Rocksalt Ordered Structures. *J. Chem. Sci.* **2015**, *127* (2), 225−233.

(8) Bhardwaj, N.; Gupta, A.; Uma, S. Evidence of Cationic Mixing and Ordering in the Honeycomb Layer of $Li_4MSbO_6$ (M(III) = Cr, Mn, Al, Ga) (S.G. C2/c) Oxides. *Dalton Trans.* **2014**, *43* (31), 12050−12057.

(9) Mather, G. C.; Dussarrat, C.; Etourneau, J.; West, A. R. A Review of Cation-Ordered Rock Salt Superstructure Oxides. *J. Mater. Chem.* **2000**, *10* (10), 2219−2230.

(10) Jacquet, Q.; Rousse, G.; Iadecola, A.; Saubanère, M.; Doublet, M.-L.; Tarascon, J.-M. Electrostatic Interactions versus Second Order Jahn−Teller Distortion as the Source of Structural Diversity in $Li_3MO_4$ Compounds (M = Ru, Nb, Sb and Ta). *Chem. Mater.* **2018**, *30* (2), 392−402.

(11) Yabuuchi, N.; Takeuchi, M.; Nakayama, M.; Shiiba, H.; Ogawa, M.; Nakayama, K.; Ohta, T.; Endo, D.; Ozaki, T.; Inamasu, T.; Sato, K.; Komaba, S. High-Capacity Electrode Materials for Rechargeable Lithium Batteries: $Li_3NbO_4$-Based System with Cation-Disordered Rocksalt Structure. *Proc. Natl. Acad. Sci. U. S. A.* **2015**, *112* (25), 7650−7655.

(12) Yabuuchi, N.; Tahara, Y.; Komaba, S.; Kitada, S.; Kajiya, Y. Synthesis and Electrochemical Properties of $Li_4MoO_5$−NiO Binary System as Positive Electrode Materials for Rechargeable Lithium Batteries. *Chem. Mater.* **2016**, *28* (2), 416−419.

(13) Croy, J. R.; Gallagher, K. G.; Balasubramanian, M.; Chen, Z.; Ren, Y.; Kim, D.; Kang, S.-H.; Dees, D. W.; Thackeray, M. M. Examining Hysteresis in Composite $xLi_2MnO_3\cdot(1-x)LiMO_2$ Cathode Structures. *J. Phys. Chem. C* **2013**, *117* (13), 6525−6536.

(14) Croy, J. R.; Balasubramanian, M.; Gallagher, K. G.; Burrell, A. K. Review of the U.S. Department of Energy's "Deep Dive" Effort to Understand Voltage Fade in Li- and Mn-Rich Cathodes. *Acc. Chem. Res.* **2015**, *48* (11), 2813−2821.

(15) Assat, G.; Foix, D.; Delacourt, C.; Iadecola, A.; Dedryvère, R.; Tarascon, J.-M. Fundamental Interplay between Anionic/Cationic Redox Governing the Kinetics and Thermodynamics of Lithium-Rich Cathodes. *Nat. Commun.* **2017**, *8* (1), 2219.

(16) Mandal, T. K.; Gopalakrishnan, J. New Route to Ordered Double Perovskites: Synthesis of Rock Salt Oxides, $Li_4MWO_6$, and Their Transformation to $Sr_2MWO_6$ (M = Mg, Mn, Fe, Ni) via Metathesis. *Chem. Mater.* **2005**, *17* (9), 2310−2316.

(17) Fletcher, J. G.; Mather, G. C.; West, A. R.; Castellanos, M.; Gutierrez, M. P. $Li_3Ni_2TaO_6$: A Novel Rock Salt Superstructure Phase with Partial Cation Order. *J. Mater. Chem.* **1994**, *4* (8), 1303−1305.

(18) Hauck, J. Short-Range Order and Superstructures of Ternary Oxides $AMO_2$, $A_2MO_3$ and $A_5MO_6$ of Monovalent A and Multivalent M Metals Related to the NaCl Structure. *Acta Crystallogr., Sect. A: Cryst. Phys., Diffr., Theor. Gen. Crystallogr.* **1980**, *36* (2), 228−237.

(19) Oh, S.-J.; Lee, D. W.; Ok, K. M. $PbMSeO_6$ (M = Mo and W): New Quaternary Mixed Metal Selenites with Asymmetric Cationic Coordination Environments. *Dalton Trans.* **2012**, *41* (10), 2995−3000.

(20) Halasyamani, P. S. Asymmetric Cation Coordination in Oxide Materials: Influence of Lone-Pair Cations on the Intra-Octahedral Distortion in $d^0$ Transition Metals. *Chem. Mater.* **2004**, *16* (19), 3586−3592.

(21) Morss, L. R.; Appelman, E. H.; Gerz, R. R.; Martin-Rovet, D. Structural Studies of $Li_5ReO_6$, $Li_4NpO_5$ and $Li_5NpO_6$ by Neutron and X-Ray Powder Diffraction. *J. Alloys Compd.* **1994**, *203*, 289−295.

(22) Sathiya, M.; Ramesha, K.; Rousse, G.; Foix, D.; Gonbeau, D.; Guruprakash, K.; Prakash, A. S.; Doublet, M. L.; Tarascon, J.-M. $Li_4NiTeO_6$ as a Positive Electrode for Li-Ion Batteries. *Chem. Commun.* **2013**, *49* (97), 11376−11378.

(23) Nguyen, P.-H. T.; Kemei, M. C.; Tan, M. S.; Derakhshan, S. Synthesis, Crystal Structure and Magnetic Properties of the Two Polymorphs of Novel S = 1 Osmate; $Li_4MgOsO_6$. *J. Solid State Chem.* **2016**, *242*, 155−160.

(24) Milam-Guerrero, J.; Bloed, C. J.; Nguyen, P.-H. T.; Tran, G. T.; Martin, W. P.; Papakostas, D. V.; Toro, J.; Wilson, M. N.; Carlo, J. P.; Luke, G. M.; Melot, B. C.; Gu, J.; Derakhshan, S. Synthesis, Crystal Structure, and Magnetic Properties of the Highly Frustrated Orthorhombic $Li_4MgReO_6$. *Inorg. Chem.* **2017**, *56* (19), 11633−11639.

(25) Koga, H.; Croguennec, L.; Ménétrier, M.; Mannessiez, P.; Weill, F.; Delmas, C. Different Oxygen Redox Participation for Bulk and Surface: A Possible Global Explanation for the Cycling Mechanism of $Li_{1.20}Mn_{0.54}Co_{0.13}Ni_{0.13}O_2$. *J. Power Sources* **2013**, *236*, 250−258.

(26) Pearce, P. E.; Perez, A. J.; Rousse, G.; Saubanère, M.; Batuk, D.; Foix, D.; McCalla, E.; Abakumov, A. M.; Van Tendeloo, G.; Doublet, M.-L.; Tarascon, J.-M. Evidence for Anionic Redox Activity in a Tridimensional-Ordered Li-Rich Positive Electrode $\beta$-$Li_2IrO_3$. *Nat. Mater.* **2017**, *16* (5), 580−586.

(27) Dahn, J. R.; von Sacken, U.; Michal, C. A. Structure and Electrochemistry of $Li_{1\pm y}NiO_2$ and a New $Li_2NiO_2$ Phase with the $Ni(OH)_2$ Structure. *Solid State Ionics* **1990**, *44* (1), 87−97.



DOI: 10.1021/jacs.8b13633
*J. Am. Chem. Soc.* 2019, 141, 7333−7346

(28) O'Grady, W. E.; Pandya, K. I.; Swider, K. E.; Corrigan, D. A. In Situ X-Ray Absorption Near-Edge Structure Evidence for Quadrivalent Nickel in Nickel Battery Electrodes. *J. Electrochem. Soc.* **1996**, *143* (5), 1613−1617.
(29) Mansour, A. N.; Melendres, C. A. Analysis of X-Ray Absorption Spectra of Some Nickel Oxycompounds Using Theoretical Standards. *J. Phys. Chem. A* **1998**, *102* (1), 65−81.
(30) Mansour, A. N.; Yang, X. Q.; Sun, X.; McBreen, J.; Croguennec, L.; Delmas, C. In Situ X-Ray Absorption Spectroscopy Study of $Li_{(1-z)}Ni_{(1+z)}O_2$ ($z \leq 0.02$) Cathode Material. *J. Electrochem. Soc.* **2000**, *147* (6), 2104−2109.
(31) Pecquenard, B.; Castro-Garcia, S.; Livage, J.; Zavalij, P. Y.; Whittingham, M. S.; Thouvenot, R. Structure of Hydrated Tungsten Peroxides $[WO_2(O_2)H_2O]\cdot nH_2O$. *Chem. Mater.* **1998**, *10* (7), 1882−1888.
(32) Campbell, N. J.; Dengel, A. C.; Edwards, C. J.; Griffith, W. P. Studies on Transition Metal Peroxo Complexes. Part 8. The Nature of Peroxomolybdates and Peroxotungstates in Aqueous Solution. *J. Chem. Soc., Dalton Trans.* **1989**, No. 6, 1203−1208.
(33) Horsley, J. A.; Wachs, I. E.; Brown, J. M.; Via, G. H.; Hardcastle, F. D. Structure of Surface Tungsten Oxide Species in the Tungsten Trioxide/Alumina Supported Oxide System from X-Ray Absorption near-Edge Spectroscopy and Raman Spectroscopy. *J. Phys. Chem.* **1987**, *91* (15), 4014−4020.
(34) Eysel, H. H.; Thym, S. Raman Spectra of Peroxides. *Z. Anorg. Allg. Chem.* **1975**, *411* (2), 97−102.
(35) Li, X.; et al. Direct Visualization of the Reversible $O^{2-}/O^{-}$ Redox Process in Li-Rich Cathode Materials. *Adv. Mater.* **2018**, *30* (14), 1705197.
(36) Qiao, Y.; Guo, S.; Zhu, K.; Liu, P.; Li, X.; Jiang, K.; Sun, C.-J.; Chen, M.; Zhou, H. Reversible Anionic Redox Activity in $Na_3RuO_4$ Cathodes: A Prototype Na-Rich Layered Oxide. *Energy Environ. Sci.* **2018**, *11* (2), 299−305.
(37) Baddour-Hadjean, R.; Pereira-Ramos, J.-P. Raman Microspectrometry Applied to the Study of Electrode Materials for Lithium Batteries. *Chem. Rev.* **2010**, *110* (3), 1278−1319.
(38) Luo, K.; Roberts, M. R.; Guerrini, N.; Tapia-Ruiz, N.; Hao, R.; Massel, F.; Pickup, D. M.; Ramos, S.; Liu, Y.-S.; Guo, J.; Chadwick, A. V.; Duda, L. C.; Bruce, P. G. Anion Redox Chemistry in the Cobalt Free 3d Transition Metal Oxide Intercalation Electrode $Li[Li_{0.2}Ni_{0.2}Mn_{0.6}]O_2$. *J. Am. Chem. Soc.* **2016**, *138* (35), 11211−11218.
(39) Sathiya, M.; Rousse, G.; Ramesha, K.; Laisa, C. P.; Vezin, H.; Sougrati, M. T.; Doublet, M.-L.; Foix, D.; Gonbeau, D.; Walker, W.; Prakash, A. S.; Ben Hassine, M.; Dupont, L.; Tarascon, J.-M. Reversible Anionic Redox Chemistry in High-Capacity Layered-Oxide Electrodes. *Nat. Mater.* **2013**, *12* (9), 827−835.
(40) Luo, K.; Roberts, M. R.; Hao, R.; Guerrini, N.; Pickup, D. M.; Liu, Y.-S.; Edström, K.; Guo, J.; Chadwick, A. V.; Duda, L. C.; Bruce, P. G. Charge-Compensation in 3d-Transition-Metal-Oxide Intercalation Cathodes through the Generation of Localized Electron Holes on Oxygen. *Nat. Chem.* **2016**, *8* (7), 684−691.
(41) Assat, G.; Tarascon, J.-M. Fundamental Understanding and Practical Challenges of Anionic Redox Activity in Li-Ion Batteries. *Nat. Energy* **2018**, *3* (5), 373−386.
(42) Assat, G.; Iadecola, A.; Delacourt, C.; Dedryvère, R.; Tarascon, J.-M. Decoupling Cationic−Anionic Redox Processes in a Model Li-Rich Cathode via Operando X-Ray Absorption Spectroscopy. *Chem. Mater.* **2017**, *29* (22), 9714−9724.
(43) Lee, J.; Seo, D.-H.; Balasubramanian, M.; Twu, N.; Li, X.; Ceder, G. A New Class of High Capacity Cation-Disordered Oxides for Rechargeable Lithium Batteries: Li−Ni−Ti−Mo Oxides. *Energy Environ. Sci.* **2015**, *8*, 3255−3265.
(44) McCalla, E.; Abakumov, A. M.; Saubanère, M.; Foix, D.; Berg, E. J.; Rousse, G.; Doublet, M.-L.; Gonbeau, D.; Novák, P.; Tendeloo, G. V.; Dominko, R.; Tarascon, J.-M. Visualization of O-O Peroxo-like Dimers in High-Capacity Layered Oxides for Li-Ion Batteries. *Science* **2015**, *350* (6267), 1516−1521.
(45) Rietveld, H. M. Line Profiles of Neutron Powder-Diffraction Peaks for Structure Refinement. *Acta Crystallogr.* **1967**, *22* (1), 151−152.
(46) Rietveld, H. M. A Profile Refinement Method for Nuclear and Magnetic Structures. *J. Appl. Crystallogr.* **1969**, *2* (2), 65−71.
(47) Ravel, B.; Newville, M. Athena, Artemis, Hephaestus: Data Analysis for X-Ray Absorption Spectroscopy Using IFEFFIT. *J. Synchrotron Radiat.* **2005**, *12* (4), 537−541.
(48) Kresse, G.; Furthmüller, J. Efficient Iterative Schemes for Ab Initio Total-Energy Calculations Using a Plane-Wave Basis Set. *Phys. Rev. B: Condens. Matter Mater. Phys.* **1996**, *54* (16), 11169−11186.
(49) Perdew, J. P.; Burke, K.; Ernzerhof, M. Generalized Gradient Approximation Made Simple. *Phys. Rev. Lett.* **1996**, *77* (18), 3865−3868.
(50) Dudarev, S. L.; Botton, G. A.; Savrasov, S. Y.; Humphreys, C. J.; Sutton, A. P. Electron-Energy-Loss Spectra and the Structural Stability of Nickel Oxide: An LSDA+U Study. *Phys. Rev. B: Condens. Matter Mater. Phys.* **1998**, *57* (3), 1505−1509.
(51) Kresse, G.; Joubert, D. From Ultrasoft Pseudopotentials to the Projector Augmented-Wave Method. *Phys. Rev. B: Condens. Matter Mater. Phys.* **1999**, *59* (3), 1758−1775.
(52) Fonari, A.; Stauffer, S. Python Program to Evaluate Off-Resonance Raman Activity Using VASP Code as the Backend; *Raman-Sc/VASP*; 2013, https://github.com/raman-sc/VASP.
(53) Dovesi, R.; Orlando, R.; Erba, A.; Zicovich-Wilson, C. M.; Civalleri, B.; Casassa, S.; Maschio, L.; Ferrabone, M.; Pierre, M. D. L.; D'Arco, P.; Noël, Y.; Causà, M.; Rérat, M.; Kirtman, B. CRYSTAL14: A Program for the Ab Initio Investigation of Crystalline Solids. *Int. J. Quantum Chem.* **2014**, *114* (19), 1287−1317.
(54) Krukau, A. V.; Vydrov, O. A.; Izmaylov, A. F.; Scuseria, G. E. Influence of the Exchange Screening Parameter on the Performance of Screened Hybrid Functionals. *J. Chem. Phys.* **2006**, *125* (22), 224106.
(55) Peintinger, M. F.; Oliveira, D. V.; Bredow, T. Consistent Gaussian Basis Sets of Triple-Zeta Valence with Polarization Quality for Solid-State Calculations. *J. Comput. Chem.* **2013**, *34* (6), 451−459.
(56) Wang, F.; Di Valentin, C.; Pacchioni, G. Electronic and Structural Properties of $WO_3$: A Systematic Hybrid DFT Study. *J. Phys. Chem. C* **2011**, *115* (16), 8345−8353.


DOI: 10.1021/jacs.8b13633
*J. Am. Chem. Soc.* 2019, 141, 7333−7346